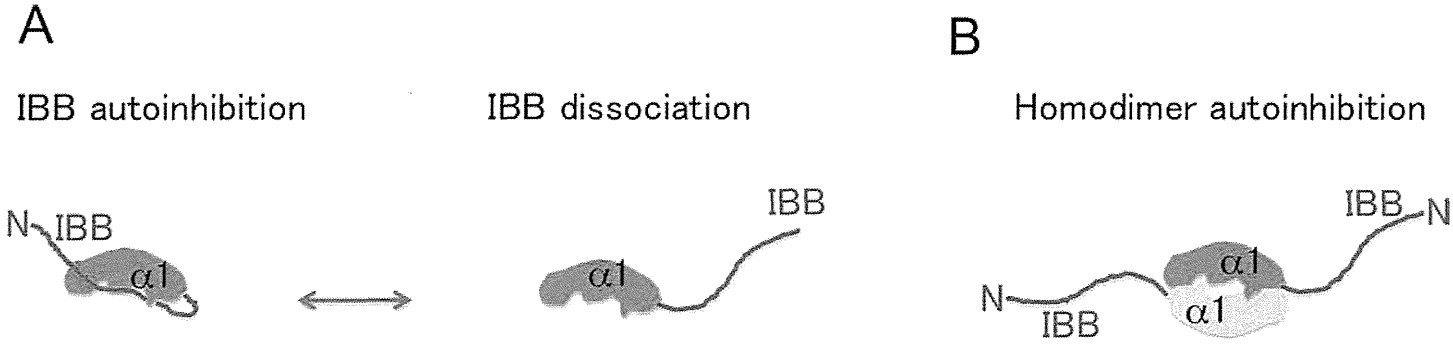

Fig 5. Autoinhibition states of h-importin-α1 by IBB binding and homodimerization. (A) A conventional scheme of autoinhibition by self-binding of IBB domain. The IBB domain bound in the NLS binding sites autoinhibits NLS binding. In addition, the current work reveals the IBB domain also prevents it from homodimerization. In turn, the bound IBB domain dissociates from the NLS binding sites by binding of NLS peptides and/or importin-β. (B) A potential homodimer autoinhibition mode. The current study reveals that a novel autoinhibition state by homodimerization, which possibly corresponds to NLS binding regulation.

doi:10.1371/journal.pone.0115995.g005

dissociation constant KD of ~20 μM [36]. We found that the *Xenopus* importin-α has an arginine residue (R105) that is aligned to the K108 of importin-α1 (S2 Fig.). Thus, the R105 possibly interacts with the P1′-binding pocket of another protomer, promoting the closed-homodimerization.

The first structural knowledge about the autoinhibition mechanism was obtained from the crystal structure of mouse-importin-α2 (m-importin-α2) [37], [38]. In that crystal structure, the IBB domain binds to the major, but not the minor, NLS binding site; thus the NLS binding affinity is partly autoinhibited. It has been unclear whether m-importin-α2 forms a homodimer or not [37], although the m-importin-α2 has a K102 and the P1′-binding pocket consists of the same residues as in h-importin-α1 (S2 Fig.). Further studies should be addressed about the multimerization property of the m-importin-α2.

It is reported that ΔIBB-h-importin-α1 (70–529) complexes with the cap-binding complex (CBC) [39]. In the ΔIBB-h-importin-α1 (70–529)-CBC complex, the NH1 and NH2 of R3 (P1′) in the canonical type of NLS (RRXX; P1′P2′XX) at the N-terminus of CBC (CBP80 + CBP20) form hydrogen bonds with OD2 of D325 and OG1 of T328 in the ridge of the P1′-binding pocket (Fig. 4E), which may shift the monomer-dimer equilibration to the monomeric side.

A possible autoinhibition state of h-importin-α1

Together with the results obtained from the AUC-SV, ITC, and crystallography, we can add a potential autoinhibition mode of the h-importin-α1 to the conventional scenario, as shown in Fig. 5. In the canonical scheme, the self-bound IBB domain autoinhibits NLS binding to the NLS binding sites in h-importin-α1. Our current study reveals that the self-bound IBB domain also autoinhibits homodimerization. The IBB domain is dissociated from the NLS binding sites, *e.g.*, by the competitive binding of NLS peptides to the NLS binding sites and/or the binding of the IBB domain to importin-β (Fig. 5A). Upon the IBB domain dissociation, the h-importin-α1 can homodimerize as an autoinhibition state (Fig. 5B), which possibly lowers the KD (~6 μM) for NLS comparing to that of yeast (~10 nM) [34]. Through the association/dissociation of the IBB domain and molecular h-importin-α1, the NLS binding to the h-importin-α1 is controlled by both of the self-binding of IBB domain and homodimerization.

Conclusions

In h-importin-α1, NLS binding affinity is autoinhibited by the self-binding of IBB domain. In addition, the closed homodimerization possibly works as an autoinhibition state when the IBB domain dissociates from the NLS binding sites. There still remains unresolved subjects whether the current closed-homodimer is physiologically relevant *in vivo*. Further studies are required to address the functional aspects of the closed-homodimer, by mutagenesis and cellular biological experiments.

Supporting Information

S1 Fig. Anion exchange chromatography with the Resource Q column and fraction characterization by 12.5% sodium dodecyl sulfate polyacrylamide gel electrophoresis (SDS-PAGE). (A) h-importin-α1. Each number assigned to the resulting elution position coincides with the lane of 12.5% SDS-PAGE. The blue line depicts the affinity column chromatography elution profile and the green line depicts the gradient of the NaCl concentration of the elution buffer. Fractions 39–44 were merged and concentrated. (B) ΔIBB-h-importin-α1. Fractions 40–45 were merged and concentrated.
(EPS)

S2 Fig. Sequence alignment of importin-αs, with residue numbers and secondary structures of h-importin-α1. Sequences of human importin-α1 (UniProtKB: P52292), mouse importin-α2 (P52293), yeast importin-α (Q02821), and *Xenopus* importin-α1 (P52171). The position of K108 of importin-α1 is represented by a blue triangle. The residues (V321, T322, D325, N361, I362, G365) involved in the P1′-binding pocket around the minor NLS binding site are conserved among the importin-αs. Thus, the P1′-binding pocket should be conserved.
(EPS)

Acknowledgments

We thank Drs. Yuuki Nakamura, Go Ueno, Takaaki Hikima, and Masaki Yamamoto for their help in collecting the X-ray diffraction data using the mail-in system at SPring-8. We thank Drs. Takehiro Suzuki and Katsuhiko Kamada for assistance with the analytical ultracentrifuge experiment. We thank Dr. Yoichi Takeda for instructing us in the ITC experiment. We are grateful to the Support Unit for Bio-material Analysis, and the RIKEN BSI Research Resources Center for help with sequence analysis and peptide synthesis.

Author Contributions

Conceived and designed the experiments: HM YA. Performed the experiments: HM AS GM YT SU. Analyzed the data: HM AS GM YT YM ND YA SU. Contributed reagents/materials/analysis tools: HM AS GM. Wrote the paper: HM YA.

References

1. Paine PL, Moore LC, Horowitz SB (1975). Nuclear envelope permeability Nature 254: 109–114. doi: 10.1038/254109a0 PMID: 1117994
2. Stoffler D, Fahrenkrogt B, Aebil U (1999). The nuclear pore complex: from molecular architecture to functional dynamics. Curr. Opin. Cell Biol. 11: 391–401. PMID: 10395558
3. Stoffler D, Goldie KN, Feja B, Aebi U (1999). Calcium-mediated structural changes of native nuclear pore complexes monitored by time-lapse atomic force microscopy. J. Mol. Biol. 287: 741–752. PMID: 10191142
4. Conti E, Izaurralde E (2001). Nucleocytoplasmic transport enters the atomic age. Curr. Opin. Cell Biol. 13: 310–319. PMID: 11343901

5. Tran EJ, Bolger TA, Wente SR (2007). Snapshot: nuclear transport. Cell, 131: 420. PMID: 17956740
6. Görlich D, Mattaji IW (1996). Nucleocytoplasmic transport. Science 271: 1513–1518. PMID: 8599106
7. Eigg EA (1997). Nucleocytoplasmic transport: signals, mechanisms and regulation. Nature 386: 779–787. PMID: 9126736
8. Weis K (1998). Importins and exportins: how to get in and out of the nucleus. Trends in Biochem. Sci. 23: 185–189.
9. Cuomo CA, Kirch SA, GyuRis J, Brent R, Oettinger MA (1994). Rch1, a protein that specifically interacts with the RAG-1 recombination-activating protein. Proc. Natl. Acad. Sci. USA 91: 6156–6160. PMID: 8016130
10. Goldfarb DS, Corbett AH., Mason DA, Harreman MT, Adam SA (2004). Importin alpha: a multipurpose nuclear-transport receptor. Trends Cell Biol. 14: 505–514. PMID: 15350979
11. Panté N, Kann M (2002). Nuclear pore complex is able to transport macromolecules with diameters of ~39 nm. Mol. Cell Biol. 13: 425–434.
12. Kamata M, Nitahara-Kasahara Y, Miyamoto Y, Yoneda Y, Aida Y (2005). Importin-α promotes passage through the nuclear pore complex of human immunodeficiency virus type 1 Vpr. J. Virol. 79: 3557–5364. PMID: 15731250
13. Conti E, Uy M, Leighton L, Blobel G, Kuriyan J (1998). Crystallographic analysis of the recognition of a nuclear localization signal by the nuclear import factor karyopherin alpha. Cell 94: 193–204. PMID: 9695948
14. Görlich D, Prehn S, Laskey RA, Hartmann E (1994). Isolation of a protein that is essential for the first step of nuclear protein import. Cell 79, 767–778. PMID: 8001116
15. Nitahara-Kasahara Y, Kamata M, Yamamoto T, Zhang X, Miyamoto Y, et al. (2007). Novel nuclear import of Vpr promoted by importin α is crucial for human immunodeficiency virus type 1 replication in macrophages. J. Viol. 81: 5284–5293.
16. Schuck P (2000). Size-distribution analysis of macromolecules by sedimentation velocity ultracentrifugation and lamm equation modelling. Biophys. J. 78: 1606–1619. PMID: 10692345
17. Schuck P (2003) On the analysis of protein self-association by sedimentation velocity analytical ultracentrifugation. Anal. Biochem. 320: 104–124. PMID: 12895474
18. Ueno G, Kanda H, Hirose R, Ida K, Kumasaka T, et al. (2006). RIKEN structural genomics beamlines at the SPring-8; high throughput protein crystallography with automated beamline operation. J Struct Funct Genomics 7: 15–22. PMID: 16645781
19. Okazaki N, Hasegawa K, Ueno G, Murakami H, Kumasaka T, et al. (2008). Mail-in data collection at SPring-8 protein crystallography beamlines. J. Synchrotron Radiat. 15: 288–291. doi: 10.1107/S0909049507064679 PMID: 18421161
20. Otwinowski Z, Minor W (1997). Processing of X-ray diffraction data collected in oscillation mode. Methods in Enzymology Macromolecular Crystallography part A 276: 307–326.
21. Keegan RM, Winn MD (2007). Automated search-model discovery and preparation for structure solution by molecular replacement. Acta Cryst. D 63: 447–457.
22. Terwilliger TC (2003). Automated main-chain model-building by template-matching and iterative fragment extension. Acta Cryst. D 59: 38–44.
23. Yao M, Zhou Y, Tanaka I (2006). Lafire: software for automating the refinement process of protein-structure analysis. Acta. Cryst. D 62: 189–196.
24. Langer G, Cohen SX, Lamzin VS, Perrakis A (2008). Automated macromolecular model building for X-ray crystallography using ARP/wARP version 7. Nat. Protoc. 3: 1171–1179. doi: 10.1038/nprot.2008.91 PMID: 18600222
25. McRee DE (1999). XtalView/Xfit—A versatile program for manipulating atomic coordinates and electron density. J. Struct. Biol. 125: 156–165. PMID: 10222271
26. Emsley P, Cowtan K(2004). Coot: model-building tools for molecular graphics. Acta Cryst. D 60: 2126–2132.
27. Brünger AT, Adams PD, Clore GM, DeLano WL, Gros P, et al. (1998). Crystallography & NMR system: a new software suite for macromolecular structure determination. Acta Cryst. D 54: 905–921.
28. Adams PD, Afonine PV, Bunkóczi G, Chen VB, Davis IW (2010). PHENIX: a comprehensive Python-based system for macromolecular structure solution. Acta Cryst. D 66: 213–221.
29. Laskowski RA (1993). PROCHECK: a program to check the stereochemical quality of protein structures. J. Appl. Cryst. 26: 283–291.

30. Davis IW, Murry LW, Richardson JS, Richardson DS (2004). Molprobity: structure validation and all-atom contact analysis for nucleic acids and their complexes. Nucleic Acids Res. 32:W615–619. PMID: 15215462

31. Fontes MR, Teh T, Kobe B (2000). Structural basis of recognition of monopartite and bipartite nuclear localization sequences by mammalian importin-α. J. Mol. Biol. 297: 1183–1194. PMID: 10764582

32. Conti E, Kuriyan J (2000). Crystallographic analysis of the specific yet versatile recognition of distinct nuclear localization signals by karyopherin α. Structure 8: 229–338.

33. Nair R, Carter P, Rost B (2003). Nlsdb: database of nuclear localization signals. Nucleic Acids Res. 31: 397–399. PMID: 12520032

34. Hodel AE, Harreman MT, Pulliam KF, Harben ME, Holmes JS, et al. (2006). Nuclear localization signal receptor affinity correlates with *in vivo* localization in *Saccharomyces cerevisiae*. J. Biol. Chem. 281: 23545–23556. PMID: 16785238

35. Fanara P, Hodel MR, Corbett AH, Hodel AE (2000). Quantitative analysis of nuclear localization signal (NLS)-importin α interaction through fluorescence depolarization evidence for auto-inhibitory regulation of NLS binding. J. Biol. Chem. 275: 21218–21223. PMID: 10806202

36. Percipalle P, Jonathan P, Butler G, Finch JT, Jans DA, et al. (1999). Nuclear localization signal recognition causes release of importin-α from aggregates in the cytosol. J. Mol. Biol. 292: 263–273. PMID: 10493874

37. Kobe B. (1999). Autoinhibition by an internal nuclear localization signal revealed by the crystal structure of mammalian importin a. Nat. Struct. Biol. 6: 388–397. PMID: 10201409

38. Kobe B. (1999). Nuclear targeting signal recognition: a key control point in nuclear transport? Nat. Struct. Biol. 6: 388–397. PMID: 10201409

39. Dias SMG, Wilson K, Rojas KF, Ambrosio ALB, Cerione RA. (2009). The molecular basis for the regulation of the cap-binding complex by the importins. Nat. Struct. Mol. Biol. 16: 930–937. doi: 10.1038/nsmb.1649 PMID: 19668212

40. DeLano WL. (2002). The PyMOL Molecular Graphics System (DeLano Scientific, San Carlos, California, USA).

OPEN ACCESS Freely available online

PLOS | PATHOGENS

APOBEC3D and APOBEC3F Potently Promote HIV-1 Diversification and Evolution in Humanized Mouse Model

Kei Sato[1☯]*, Junko S. Takeuchi[1☯], Naoko Misawa[1], Taisuke Izumi[2¤a], Tomoko Kobayashi[1¤b], Yuichi Kimura[1], Shingo Iwami[3], Akifumi Takaori-Kondo[4], Wei-Shau Hu[5], Kazuyuki Aihara[6,7], Mamoru Ito[8], Dong Sung An[9,10,11], Vinay K. Pathak[2], Yoshio Koyanagi[1]

1 Laboratory of Viral Pathogenesis, Institute for Virus Research, Kyoto University, Kyoto, Kyoto, Japan, **2** Viral Mutation Section, HIV Drug Resistance Program, Center for Cancer Research, National Cancer Institute-Frederick, Frederick, Maryland, United States of America, **3** Department of Biology, Faculty of Sciences, Kyushu University, Fukuoka, Fukuoka, Japan, **4** Department of Hematology and Oncology, Graduate School of Medicine, Kyoto University, Kyoto, Kyoto, Japan, **5** Viral Recombination Section, HIV Drug Resistance Program, Center for Cancer Research, National Cancer Institute-Frederick, Frederick, Maryland, United States of America, **6** Institute of Industrial Science, The University of Tokyo, Meguro-ku, Tokyo, Japan, **7** Graduate School of Information Science and Technology, The University of Tokyo, Meguro-ku, Tokyo, Japan, **8** Central Institute for Experimental Animals, Kawasaki, Kanagawa, Japan, **9** Division of Hematology and Oncology, University of California, Los Angeles, Los Angeles, California, United States of America, **10** School of Nursing, University of California, Los Angeles, Los Angeles, California, United States of America, **11** AIDS Institute, University of California, Los Angeles, Los Angeles, California, United States of America

Abstract

Several APOBEC3 proteins, particularly APOBEC3D, APOBEC3F, and APOBEC3G, induce G-to-A hypermutations in HIV-1 genome, and abrogate viral replication in experimental systems, but their relative contributions to controlling viral replication and viral genetic variation *in vivo* have not been elucidated. On the other hand, an HIV-1-encoded protein, Vif, can degrade these APOBEC3 proteins via a ubiquitin/proteasome pathway. Although APOBEC3 proteins have been widely considered as potent restriction factors against HIV-1, it remains unclear which endogenous APOBEC3 protein(s) affect HIV-1 propagation *in vivo*. Here we use a humanized mouse model and HIV-1 with mutations in Vif motifs that are responsible for specific APOBEC3 interactions, DRMR/AAAA (4A) or YRHHY/AAAAA (5A), and demonstrate that endogenous APOBEC3D/F and APOBEC3G exert strong anti-HIV-1 activity *in vivo*. We also show that the growth kinetics of 4A HIV-1 negatively correlated with the expression level of APOBEC3F. Moreover, single genome sequencing analyses of viral RNA in plasma of infected mice reveal that 4A HIV-1 is specifically and significantly diversified. Furthermore, a mutated virus that is capable of using both CCR5 and CXCR4 as entry coreceptor is specifically detected in 4A HIV-1-infected mice. Taken together, our results demonstrate that APOBEC3D/F and APOBEC3G fundamentally work as restriction factors against HIV-1 *in vivo*, but at the same time, that APOBEC3D and APOBEC3F are capable of promoting viral diversification and evolution *in vivo*.

Citation: Sato K, Takeuchi JS, Misawa N, Izumi T, Kobayashi T, et al. (2014) APOBEC3D and APOBEC3F Potently Promote HIV-1 Diversification and Evolution in Humanized Mouse Model. PLoS Pathog 10(10): e1004453. doi:10.1371/journal.ppat.1004453

Editor: Susan R. Ross, University of Pennsylvania School of Medicine, United States of America

Received June 23, 2014; **Accepted** September 5, 2014; **Published** October 16, 2014

Data Availability: The authors confirm that all data underlying the findings are fully available without restriction. All relevant data are within the paper and its Supporting Information files.

Funding: This study was supported in-part by grants from the following: the Aihara Innovative Mathematical Modelling Project, JSPS through the "Funding Program for World-Leading Innovative R&D on Science and Technology (FIRST Program)," initiated by the Council for Science and Technology Policy of Japan (to KS, SI, and KA); Grants-in-Aid for Scientific Research B24390112 (to YKo) and S22220007 (to MI and YKo) and a Grant-in-Aid for Young Scientists B23790500 (to KS) from the Japan Society for the Promotion of Science (JSPS); a Grant-in-Aid for Scientific Research on Innovative Areas 24115008 (to YKo) from the Ministry of Education, Culture, Sports, Science and Technology of Japan, Research on HIV/AIDS (to YKo) from the Ministry of Health, Labor and Welfare of Japan; Takeda Science Foundation (to KS); Sumitomo Foundation Research Grant (to KS); Senshin Medical Research Foundation (to KS); Imai Memorial Trust for AIDS Research (to KS); JST PRESTO program (to SI); and a UCLA CFAR grant 5P30AI028697 (to DSA); JSPS Research Fellowship for Japanese Biomedical and Behavioral Researchers at NIH (to TI); and the Intramural Research Program of the NIH, National Cancer Institute, Center for Cancer Research (to VKP). The content of this publication does not necessarily reflect the views or policies of the Department of Health and Human Services, nor does mention of trade names, commercial products, or organizations imply endorsement by the U.S. Government. The funders had no role in study design, data collection and analysis, decision to publish, or preparation of the manuscript.

Competing Interests: The authors declare that no competing interests exist.

* Email: ksato@virus.kyoto-u.ac.jp

☯ These authors contributed equally to this work.

¤a Current address: Department of Microbiology, Institute of Health Biosciences, The University of Tokushima, Tokushima, Japan
¤b Current address: Laboratory of Animal Health, Department of Animal Science, Faculty of Agriculture, Tokyo University of Agriculture, Atsugi, Kanagawa, Japan

Introduction

Activation-induced cytidine deaminase/apolipoprotein B mRNA editing enzyme, catalytic polypeptide-like (AID/APOBEC) superfamily is composed of cellular cytidine deaminases that closely associate with crucial events in vertebrates such as immunity, malignancy, metabolism, and infectious diseases [1,2]. For instance, AID causes somatic hypermutation in B cells resulting in antibody diversification [2], whereas APOBEC1 edits the mRNA of apolipoprotein B and regulates lipid metabolism [3].

Author Summary

Mutation can produce three outcomes in viruses: detrimental, neutral, or beneficial. The first one leads to abrogation of virus replication because of error catastrophe, while the last one lets the virus escape from anti-viral immune system or adapt to the host. Human APOBEC3D, APOBEC3F, and APOBEC3G are cellular cytidine deaminases which cause G-to-A mutations in HIV-1 genome. Here we use a humanized mouse model and demonstrate that endogenous APOBEC3F and APOBEC3G induce G-to-A hypermutation in viral genomes and exert strong anti-HIV-1 activity *in vivo*. We also reveal that endogenous APOBEC3D and/or APOBEC3F induce viral diversification, which can lead to the emergence of a mutated virus that converts its coreceptor usage. Our results suggest that APOBEC3D and APOBEC3F are capable of promoting viral diversification and functional evolution *in vivo*.

The paralogs of human *AID*, *APOBEC1*, and *APOBEC2* genes are encoded in rodents and artiodactyls [4]. On the other hand, although mice encode a sole *Apobec3* gene, primates encode seven paralogs of murine *Apobec3* in their genome, which are designated to *APOBEC3A* to *H*. Given the strong evidence that the duplicated genes have been exposed to selective pressures [5], the seven *APOBEC3* genes have been positively selected [6] and APOBEC3 family proteins play various roles in primates including humans. For instance, APOBEC3A initiates the mutations of foreign DNA (e.g., microbial DNA), which leads to the clearance of bacteria from human cells [7]. In addition, APOBEC3B-mediated mutation closely associates with several human cancers [8,9], particularly breast cancer [10].

APOBEC3G is the most extensively studied APOBEC3 protein in the field of virology and plays a crucial role in the infection and replication of HIV-1, a causative agent of AIDS [11]. APOBEC3G is incorporated into HIV-1 particles and induces G-to-A mutations in the newly synthesized viral DNA, which results in the abrogation of viral replication [4,12]. On the other hand, an HIV-1-encoded protein, viral infectivity factor (Vif), impedes APOBEC3G incorporation into progeny virions by degrading these proteins through the ubiquitin/proteasome-dependent pathway [4,12]. In addition to APOBEC3G, *in vitro* studies using cell culture systems have demonstrated that like APOBEC3G, APOBEC3F and APOBEC3D also potently impair HIV-1 replication [13–15]. However, one study has concluded that APOBEC3F expression levels in T cell lines were not sufficient to inhibit HIV-1 replication [16]. Another study analyzed the replication of HIV-1 Vif mutants that were defective in inducing degradation of APOBEC3G or APOBEC3F in primary $CD4^+$ T cells, and concluded that APOBEC3G exerts a stronger antiviral activity on HIV-1 than APOBEC3F [17]. Thus, the relative impact of different APOBEC3 proteins on HIV-1 replication *in vivo* has not been determined.

Apart from their anti-HIV-1 abilities, certain studies have suggested that APOBEC3-mediated G-to-A mutation can lead to viral evolution and divergence [18–21]. However, it remains unclear how and which endogenous APOBEC3 proteins affect HIV-1 replication, pathogenesis, and diversity *in vivo*.

In order to elucidate the dynamics of HIV-1 infection *in vivo*, we have constructed a humanized mouse model by xenotransplanting human $CD34^+$ hematopoietic stem cells (hHSCs) into an immunodeficient NOD/SCID *Il2rg*$^{-/-}$ (NOG) mouse [22–28]. Our humanized mouse model is able to recapitulate the characteristics of HIV-1 pathogenesis such as the depletion of peripheral $CD4^+$ T cells [22,23,25]. By using this model, we have previously demonstrated that the expression levels of endogenous APOBEC3 genes in human $CD4^+$ T cells of humanized mice were comparable to those of humans and that the combined activity of endogenous APOBEC3 proteins can potently abrogate *vif*-deficient HIV-1 propagation *in vivo* [23]. However, which endogenous APOBEC3 proteins are crucial to the anti-HIV-1 effect *in vivo* is not yet known. In fact, although G-to-A mutations, presumably caused by endogenous APOBEC3 proteins, have been clearly observed in the viral genomes of HIV-1-infected patients, the frequencies of G-to-A mutations seem to vary among individuals and the mutation context is still controversial [21,29–37]. Moreover, because there is a possibility that some endogenous APOBEC3 protein(s) are capable of facilitating viral diversification *in vivo*, it is important to elucidate how endogenous APOBEC3 proteins would affect HIV-1 if we target these molecules for therapy.

In this study, we demonstrate that the propagation of HIV-1 *vif* mutants, which are unable to degrade APOBEC3D/F, APOBEC3G, or both APOBEC3D/F and APOBEC3G, are severely impaired, demonstrating that endogenous APOBEC3D/F and APOBEC3G proteins potently suppress HIV-1 propagation *in vivo*. In addition to the anti-HIV-1 activity of APOBEC3D and APOBEC3F, our results demonstrate that endogenous APOBEC3D and APOBEC3F also potently induced viral diversification. Taken together, our findings show APOBEC3D and APOBEC3F promote HIV-1 diversification *in vivo* and thereby facilitate viral adaptation and evolution.

Results

Strong inhibition of HIV-1 propagation *in vivo* by mutating ^{14}DRMR^{17} and/or ^{40}YRHHY^{44} motifs in Vif

It was demonstrated that ^{14}DRMR^{17} motif in Vif is necessary for the degradation of APOBEC3D and APOBEC3F, while ^{40}YRHHY^{44} motif in Vif is necessary for the degradation of APOBEC3G [38,39]. As shown in Figure 1A, these two motifs were highly conserved in HIV-1 group M. In addition, these motifs are located on the outside regions of Vif protein (Figure 1B) [39]. Moreover, we confirmed that APOBEC3D, APOBEC3F, and APOBEC3G have the ability to decrease *vif*-deficient HIV-1 infectivity *in vitro* (Figure S1).

To confirm the importance of these motifs *in vivo*, we prepared 3 Vif mutants, DRMR/AAAA (4A), YRHHY/AAAAA (5A), and a double mutant (4A5A), based on a CCR5-tropic HIV-1 infectious molecular clone (IMC; strain NLCSFV3) [40]. As previously reported [17], the infectivity of WT, 4A, 5A, and 4A5A HIV-1s were comparable in the absence of APOBEC3s (Figure 1C). On the other hand, the infectivity of 4A HIV-1 was strongly suppressed by APOBEC3D and APOBEC3F but not by APOBEC3G, while that of 5A HIV-1 was decreased by APOBEC3G but not by APOBEC3D and APOBEC3F (Figure 1C). These results indicate that 4A HIV-1 is sensitive to APOBEC3D and APOBEC3F but not to APOBEC3G, while 5A HIV-1 is sensitive to APOBEC3G but not to APOBEC3D and APOBEC3F.

To investigate the anti-HIV-1 activity of each endogenous A3 protein *in vivo*, we inoculated WT, 4A, 5A, and 4A5A HIV-1s into humanized mice. As shown in Figure 2A, the viral loads (VLs) of 4A, 5A, and 4A5A HIV-1s were significantly lower than that of WT HIV-1, and the gradual decrease of peripheral $CD4^+$ T cells was observed only in WT HIV-1-infected mice (Figure 2B). In contrast to *vif*-deleted viruses that did not replicate at all in humanized mouse models [23,41], 4A, 5A and 4A5A HIV-1s

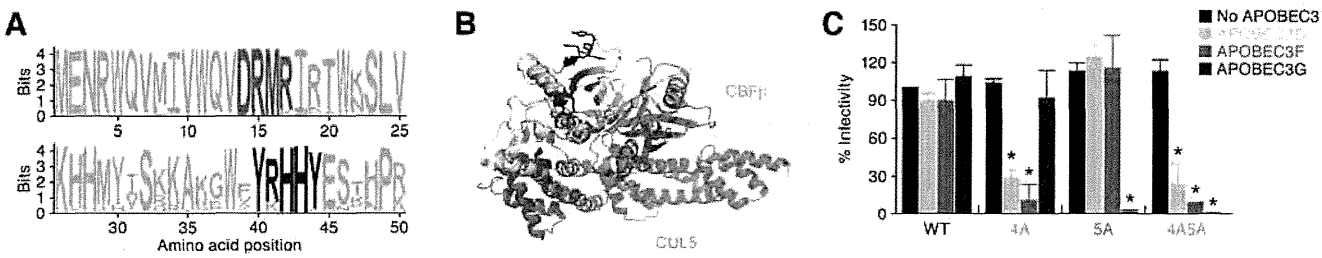

Figure 1. Anti-HIV-1 effect of APOBEC3 proteins *in vitro*. (A) Conservation of ^{14}DRMR^{17} and ^{40}YRHHY^{44} motifs in Vif. The *vif* ORF sequences of HIV-1 group M that are registered in Los Alamos HIV sequence database (n = 7,118) were aligned and analyzed as described in Materials and Methods. (B) Location of DRMR and YRHHY motifs in Vif crystal structure. The 3D structure of Vif was generated on PyMOL v1.6 (http://www.pymol.org/) with the crystal structure of Vif-CBFβ-CUL5-ELOB-ELOC complex (PDB code: 4N9F) [79]. Yellow, cyan, and magenta cartoons respectively represent the main chain of Vif, CBFβ, and CUL5. Red and blue cartoons respectively represent DRMR and YRHHY motifs in Vif. (C) TZM-bl assay. The infectivity of released virions was determined by using TZM-bl cells. The infectivity of each virus is normalized to the value of WT HIV-1 without APOBEC3. The assay was performed in triplicate. *$P<0.05$ versus no APOBEC3 by Student's *t* test. The assay was performed in triplicate. The data represents average with SD.
doi:10.1371/journal.ppat.1004453.g001

exhibited partial viremia (VL at 6 weeks postinfection [wpi]: WT HIV-1, $6.3\times10^5\pm3.0\times10^5$ copies/ml; 4A HIV-1, $1.2\times10^5\pm1.2\times10^5$ copies/ml; 5A HIV-1, $2.9\times10^3\pm0.9\times10^3$ copies/ml; 4A5A HIV-1 $2.3\times10^3\pm0.7\times10^3$ copies/ml). These suggest that the *vif*-mutated viruses used in this study retain some Vif activity, even though they are highly defective. We also inoculated higher doses of viruses into humanized mice; however, despite the higher virus dose, these HIV-1 *vif* mutants did not propagate efficiently *in vivo* (Figures S2A and S2B). These findings strongly suggest that endogenous APOBEC3 proteins, particularly APOBEC3D, APOBEC3F and APOBEC3G, can potently impair HIV-1 propagation *in vivo*.

To quantitatively analyze the magnitude of viral propagation *in vivo*, we evaluated the area under the curve (AUC) of VL (Figure 2C; see also Materials and Methods) and the virus replication rate (Figure 2D; see also Materials and Methods). As shown in Figures 2C and 2D, these two analyses revealed that both the AUC and virus replication rate of WT HIV-1 were significantly higher than those of 4A, 5A, and 4A5A HIV-1s (AUC: WT HIV-1, 10.0 ± 1.8; 4A HIV-1, 2.9 ± 0.7; 5A HIV-1, 1.1 ± 0.3; 4A5A HIV-1, 0.9 ± 0.2. Virus replication rate: WT HIV-1, 15.0 ± 3.0; 4A HIV-1, 4.9 ± 0.8; 5A HIV-1, 2.4 ± 0.4; 4A5A HIV-1, 2.6 ± 0.4). In addition, although the differences in viral load (Figure 2A) and CD4 decline (Figure 2B) between 4A and 5A HIV-1-infected mice were not large, we detected statistically significant differences between 4A and 5A HIV-1-infected mice in AUC (3.8-fold, $P=0.030$; Figure 2C) and virus replication rate (2.1-fold, $P=0.0050$; Figure 2D), respectively. Taken together, these findings suggest that endogenous APOBEC3G, APOBEC3F and/or APOBEC3D have the potential to diminish HIV-1 propagation *in vivo* and that the antiviral activity of endogenous APOBEC3G is higher than the combined antiviral activity of APOBEC3D and APOBEC3F.

No reversion of mutations in HIV-1 *vif* mutants

Although the growth of HIV-1 *vif* mutants was generally low, certain mice infected with 4A HIV-1 exhibited moderate levels of viremia (Figure 2A). To assess the possibility that reversion of mutations in *vif* led to the limited spread of HIV-1 *vif* mutants in humanized mice, we analyzed the *vif* mRNA sequences in the spleen of infected mice at 6 wpi. We observed prominent G-to-A mutations in HIV-1 *vif* mutant-infected mice (Figures S3A and S3B). We then asked whether nonsynonymous Vif mutants frequently identified in infected mice (Figure S3C) maintained their ability to degrade APOBEC3 proteins. As shown in Figure 2E, all Vif mutants were expressed at similar levels. However, although some minor variants in 4A HIV-1-infected mice such as K34E (3/320), E88K (5/320), and E134K (9/320) lost their-anti-APOBEC3G activity, all Vif mutants isolated from 4A HIV-1-infected mice were unable to eliminate APOBEC3F, and those from 5A HIV-1-infected mice were unable to eliminate APOBEC3G (Figure 2F). Although I128L mutant (ATA-to-TTA mutation) was predominantly observed in a 4A HIV-1-infected mouse (62 out of the 320 sequences analyzed; Figure S3C), this mutation did not affect its anti-APOBEC3 activity (Figure 2F). These results indicate that the *vif* mutations did not revert the 4A and 5A mutant phenotypes in infected mice, and that the moderate levels of viremia observed in some HIV-1 *vif* mutant-infected mice was not due to the restoration of Vif function.

Negative correlation between the expression level of APOBEC3F and the growth of 4A HIV-1

In the 3 kinds of HIV-1 *vif* mutants, it was noteworthy that the VL in each 4A HIV-1-infected mouse varied between individual mice, while those in 5A and 4A5A HIV-1-infected mice were uniformly low (Figure 3A, left panel). In fact, the coefficient of variance of peak VL, which indicates the extent of distribution, in 4A HIV-1-infected mice was ~2-fold higher than that in WT, 5A, and 4A5A HIV-1-infected mice (Figure 3A, right panel). These findings raised a possibility that the level of viremia in 4A HIV-1-infected mice is correlated with endogenous *APOBEC3* expression levels. To address this possibility, we determined the endogenous expression levels of *APOBEC3D*, *APOBEC3F*, and *APOBEC3G* in the spleen of humanized mice by real-time RT-PCR and standardized them to those of *APOBEC3D* according to the procedure reported previously [42,43]. Since we have previously demonstrated that the spleen is one of the major tissues for HIV-1 replication in our hHSC-transplanted humanized mouse model [25], we assumed that the endogenous expression levels of *APOBEC3* genes in the splenic human mononuclear cells (MNCs) affect the kinetics of 4A HIV-1 growth. As shown in Figure 3B, the expression levels of *APOBEC3F* and *APOBEC3G* were 6.4-fold and 24.7-fold higher than those of *APOBEC3D*, respectively, and the expression level of *APOBEC3G* was 3.9-fold higher than that of *APOBEC3F*.

We then analyzed the endogenous expression level of each *APOBEC3* gene in infected mice. Consistent with a previous study in $CD4^+$ T cell cultures *in vitro* [43], WT HIV-1 infection significantly enhanced the mRNA expression of *APOBEC3D*,

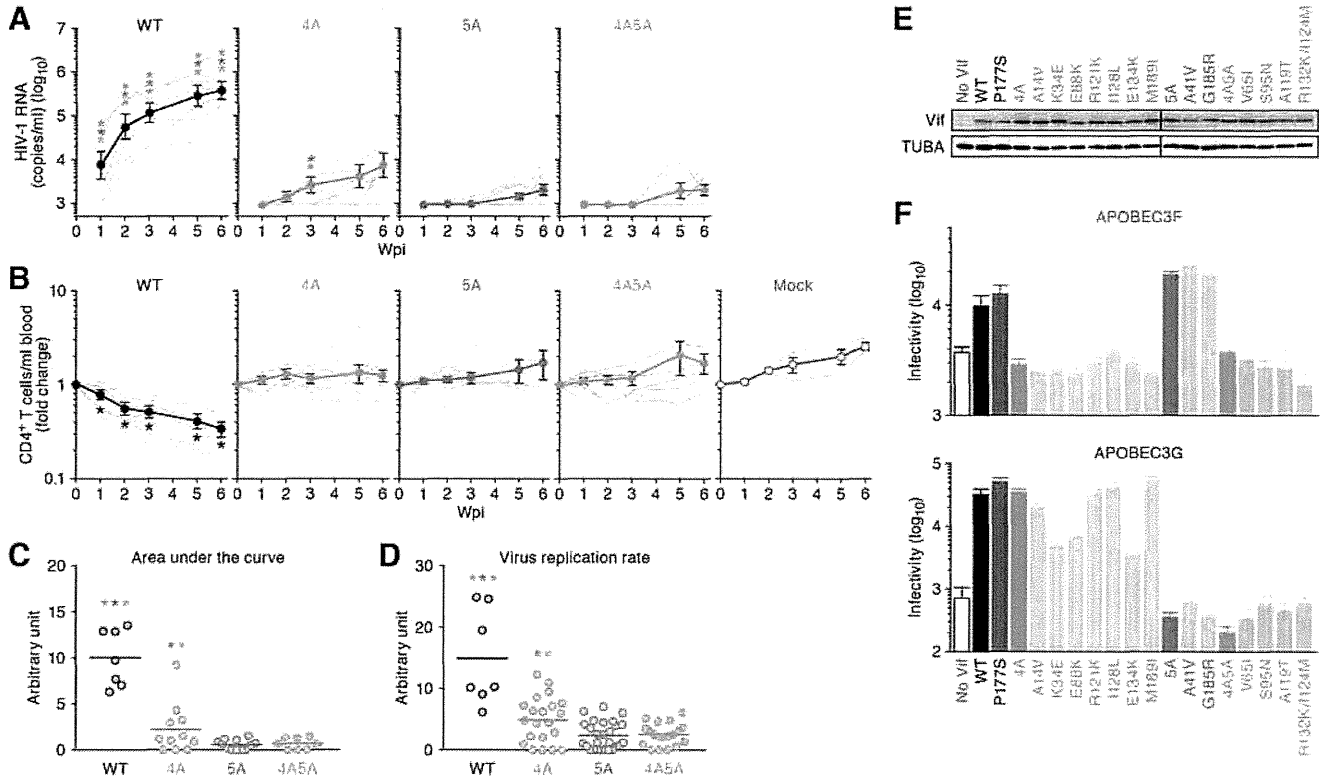

Figure 2. Dynamics of HIV-1 *vif* mutant infection in humanized mice. (A and B) The virus solutions containing 5 ng of p24 antigen (WT HIV-1 [n = 7], 4A HIV-1 [n = 11], 5A HIV-1 [n = 12], and 4A5A HIV-1 [n = 8]) or RPMI 1640 (n = 3; for mock infection) were inoculated into humanized mice, and the amount of viral RNA in plasma (A) and the level of peripheral $CD4^+$ T cells ($CD45^+$ $CD3^+$ $CD4^+$ cells) (B) were analyzed at 0, 1, 2, 3, 5, and 6 wpi. The averages are shown in circles with SEMs, and the values from each mouse are shown by line. X-axes, wpi. In panel A, the detection limit of HIV-1 RNA is 800 copies/ml plasma. (C) Area under the curve (AUC). AUCs of the VL of the mice infected with WT HIV-1 (n = 7), 4A HIV-1 (n = 11), 5A HIV-1 (n = 12), 4A5A HIV-1 (n = 8) were calculated using the trapezoidal rule as described in Materials and Methods. (D) Virus replication rate. Virus replication rates of WT HIV-1 (n = 7), 4A HIV-1 (n = 21), 5A HIV-1 (n = 27), and 4A5A HIV-1 (n = 19) were estimated by using the data of VL and peripheral $CD4^+$ T cell counts as described in Materials and Methods. In panels C and D, horizontal bars represent the averages. Asterisks represent statistically significant differences ($P<0.05$ by Student's *t* test) versus each HIV-1 *vif* mutant (A), between WT HIV-1 and *vif* mutants (C and D), and between infected mice and mock-infected mice (B). In panels A, C, and D, each color of asterisk represents the statistically significant difference against each HIV-1 *vif* mutant-infected mice. (E and F) No Vif reversion in HIV-1 *vif* mutant-infected humanized mice. (E) Western blotting of the Vif mutants frequently observed in infected mice (see also Figure S3). The input of cell lysate was standardized to α-Tubulin (TUBA), and representative results are shown. (F) TZM-bl assay. The expression plasmids of the Vif mutants were cotransfected with pNLCSFV3*Δvif* and either APOBEC3F (*top*) or APOBEC3G (*bottom*) expression plasmids into 293T cells, and the infectivity of released virus was determined by using TZM-bl cells. The assay was performed in triplicate. The data represents average with SD.
doi:10.1371/journal.ppat.1004453.g002

APOBEC3F, and *APOBEC3G* (Figure 3C). Given that HIV-1 infection induces type I interferon (IFN) production in *in vitro* cell cultures [44] and infected individuals during the acute phase [45], taken together with the fact that type I IFNs potently enhance the expression of APOBEC3 genes [42,46], we further evaluated the expression level of *IFNB*, a type I IFN. As shown in Figure 3C, the level of *IFNB* in WT HIV-1-infected mice is also significantly higher than that in mock-infected mice, although the levels of *APOBEC3D*, *APOBEC3F*, *APOBEC3G* and *IFNB* in HIV-1 *vif* mutant infected mice were comparable to mock-infected mice. Moreover, the expression levels of respective *APOBEC3* (Figure S4A) and *IFNB* (Figure S4B) were significantly correlated with each other. These findings suggest that HIV-1 propagation induces type I IFN production resulting in the augmentation of *APOBEC3* expression in humanized mice. In addition to type I IFNs, it has been reported that certain cytokines such as interleukin-2, 7, and 15 [47] and mitogens [43] also potently enhance *APOBEC3* expression. Therefore, the enhancement of *APOBEC3* expression observed in infected humanized mice (Figure 3C) might be a combination effect of type I IFNs and the other factors.

Furthermore, we assessed the relationship between the *APOBEC3* expression level and 4A HIV-1 growth kinetics and found that the VLs in 4A HIV-1-infected mice negatively correlated with the expression level of *APOBEC3F* but not of *APOBEC3D* with statistical significance (Figure 3D; $r = -0.571$, $P = 0.009$). Taken together, these results suggest that the endogenous expression level of *APOBEC3F* determines the growth kinetics of 4A HIV-1 *in vivo*.

Distinct mutation signatures observed in HIV-1 *vif* mutant-infected humanized mice

To analyze the impact of APOBEC3-mediated mutations on the viral genome *in vivo*, we performed semiquantitative differential DNA denaturation PCR (3D-PCR) [48]. In this assay, if G-to-A mutations have accumulated in an amplicon, a PCR product can be detected even at lower denaturation temperatures because the decreased GC content in the amplicon leads to more

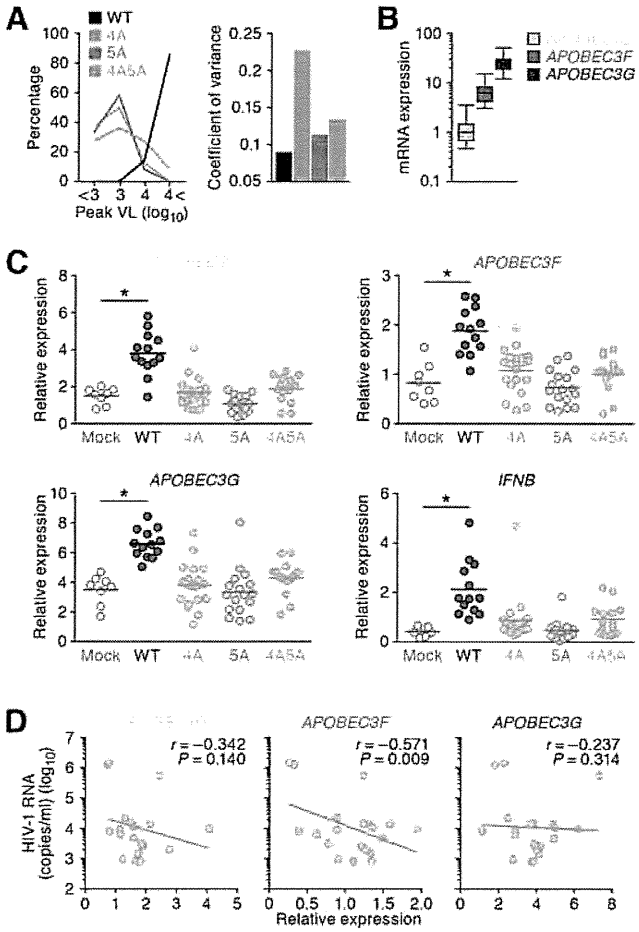

Figure 3. Expression levels of *APOBEC3* and *IFNB* in infected humanized mice. (A) Dispersion of HIV-1 growth efficiency in humanized mice. (*Left*) The peak VLs of WT HIV-1 (n = 7), 4A HIV-1 (n = 11), 5A HIV-1 (n = 12), and 4A5A HIV-1 (n = 8) were classified into 4 degrees (less than 10^3, 10^3–10^4, 10^4–10^5, or more than 10^5), and the distribution is plotted. (*Right*) The coefficient of variance of the peak VLs of WT HIV-1 (n = 7), 4A HIV-1 (n = 11), 5A HIV-1 (n = 12), and 4A5A HIV-1 (n = 8) is shown. (B) Expression levels of *APOBEC3D*, *APOBEC3F*, and *APOBEC3G* in the splenic human $CD4^+$ T cells of humanized mice (n = 73) were analyzed by real-time RT-PCR. The values were standardized as previously described [43], and the level of *APOBEC3D* is set to 1 to facilitate comparison. (C) Expression levels of *APOBEC3D*, *APOBEC3F*, *APOBEC3G*, and *IFNB* in the splenic human $CD4^+$ T cells of infected mice (WT, n = 13; 4A, n = 20; 5A, n = 17; and 4A5A, n = 15) and mock-infected mice (n = 8) at 6 wpi were analyzed by real-time RT-PCR. Horizontal bars represent the averages. Asterisks represent statistically significant difference ($P<0.05$ by Student's *t* test) between infected mice and mock-infected mice. (D) Negative correlation between VL and *APOBEC3* expression in 4A HIV-1-infected humanized mice. The mRNA expression levels of *APOBEC3D* (*left*), *APOBEC3F* (*middle*), and *APOBEC3G* (*right*) in the splenic human $CD4^+$ T cells (x-axes) and the VL at 6 wpi (y-axis) of 4A HIV-1-infected mice (n = 20) are shown. The lines represent exponential approximation. Pearson correlation coefficient (*r*) was adopted to determine statistically significant correlation between each value.

doi:10.1371/journal.ppat.1004453.g003

efficient denaturation at lower temperatures [48,49]. As shown in Figure 4A, the 3D-PCR products were detected at relatively lower denaturation temperatures in HIV-1 *vif* mutants but not of WT HIV-1, suggesting that the proviral genomes of HIV-1 *vif* mutants suffered from APOBEC3-mediated G-to-A hypermutation *in vivo*.

It is known that APOBEC3G predominantly generates GG-to-AG mutations, while APOBEC3D and APOBEC3F predominantly generate GA-to-AA mutations [14]. We assessed the sequence of full-length proviral DNA in the spleen of infected mice at 6 wpi, and found that GA-to-AA hypermutation was frequently observed in 4A HIV-1, while GG-to-AG hypermutation was readily observed in 5A and 4A5A HIV-1s (Figures 4B and 4C).

We then assessed the effect of G-to-A mutation detected in the proviral DNA of infected mice. As shown in Figure 4D, the results revealed that the percentage of termination codon mutations in 4A HIV-1 (9.3%) was significantly lower than those in 5A HIV-1 (23.8%) and 4A5A HIV-1 (21.3%) (4A HIV-1 versus 5A HIV-1, $P = 0.62\times10^{-9}$; 4A HIV-1 versus 4A5A HIV-1, $P = 0.41\times10^{-6}$ by Chi-square test for independence). Similar results were observed in the longer viral genes such as *gag*, *pol*, and *env* (Figure 4E). These results strongly suggest that APOBEC3G efficiently generates termination codons compared to APOBEC3D and APOBEC3F.

To investigate the trend of G-to-A mutation sites in depth, we verified the nucleotides positioned between −5 to +5 from the G-to-A mutation sites in the proviral DNA. Comparing the observed mutations to the expected random G-to-A mutations (shown as "reference" in Figure 4F), statistical analyses revealed that the mutation signature of 4A HIV-1-infected mice is GAA-to-AAA, while those of 5A and 4A5A HIV-1-infected mice were TGGG-to-TAGG (Figures 4F and S5A). Moreover, *in vitro* single-round infection assays revealed that the mutation signatures of APOBEC3D, APOBEC3F, and APOBEC3G were GA-to-AA, GAA-to-AAA, and TGGG-to-TAGG, respectively (Figure 4G). These results indicate that the mutation signature observed in 4A HIV-1-infected was statistically similar to those of APOBEC3D and/or APOBEC3F, and that those in 5A and 4A5A HIV-1-infected mice were statistically similar to that of APOBEC3G (Figure S5B).

Diversification of 4A HIV-1 *in vivo*

Our findings in both *in vivo* (Figure 4F) and *in vitro* (Figure 4G) demonstrated that APOBEC3G prefers to target TGGG as substrate. Importantly, TGG and TAG are the codons encoding Tryptophan and termination codon, respectively, suggesting that APOBEC3G can readily cause lethal mutations (i.e., TGG-to-TAG termination mutations). On the other hand, APOBEC3F and APOBEC3D generated GAA-to-AAA and GA-to-AA mutations, respectively (Figures 4F and 4G), which do not generate termination codons and thus cause lethal mutations less frequently. These findings raised a hypothesis that APOBEC3G directly causes lethal mutations, while APOBEC3F and APOBEC3D induce the accumulation of nonsynonymous mutations in the viral genome. To address this hypothesis, single genome sequencing (SGS) assays [50] were performed using viral RNA isolated from the plasma of infected mice at 6 wpi. Since G-to-A mutations were frequently observed in the proximal upstream region of the 3′ polypurine tract (positioned at 9056–9071; Figure S6), which was consistent with previous reports [49,51], we focused on the *env* open reading frame (ORF) sequence. As shown in Figure 5A (the raw data is shown in Figure S7), SGS assay revealed that G-to-A mutations were frequently observed in the viral RNA genomes of 4A HIV-1-infected mice but not of WT, 5A, and 4A5A HIV-1-infected mice. In addition, in the 91 *env* amplicons of 4A HIV-1-infected mice, 37 analyzed amplicons harbored more than 10 G-to-A mutations, and 15 analyzed amplicons harbored more than 10 GA-to-AA mutations, respectively (Figure S8). On the other hand, the amplicons harboring G-to-A hypermutations were

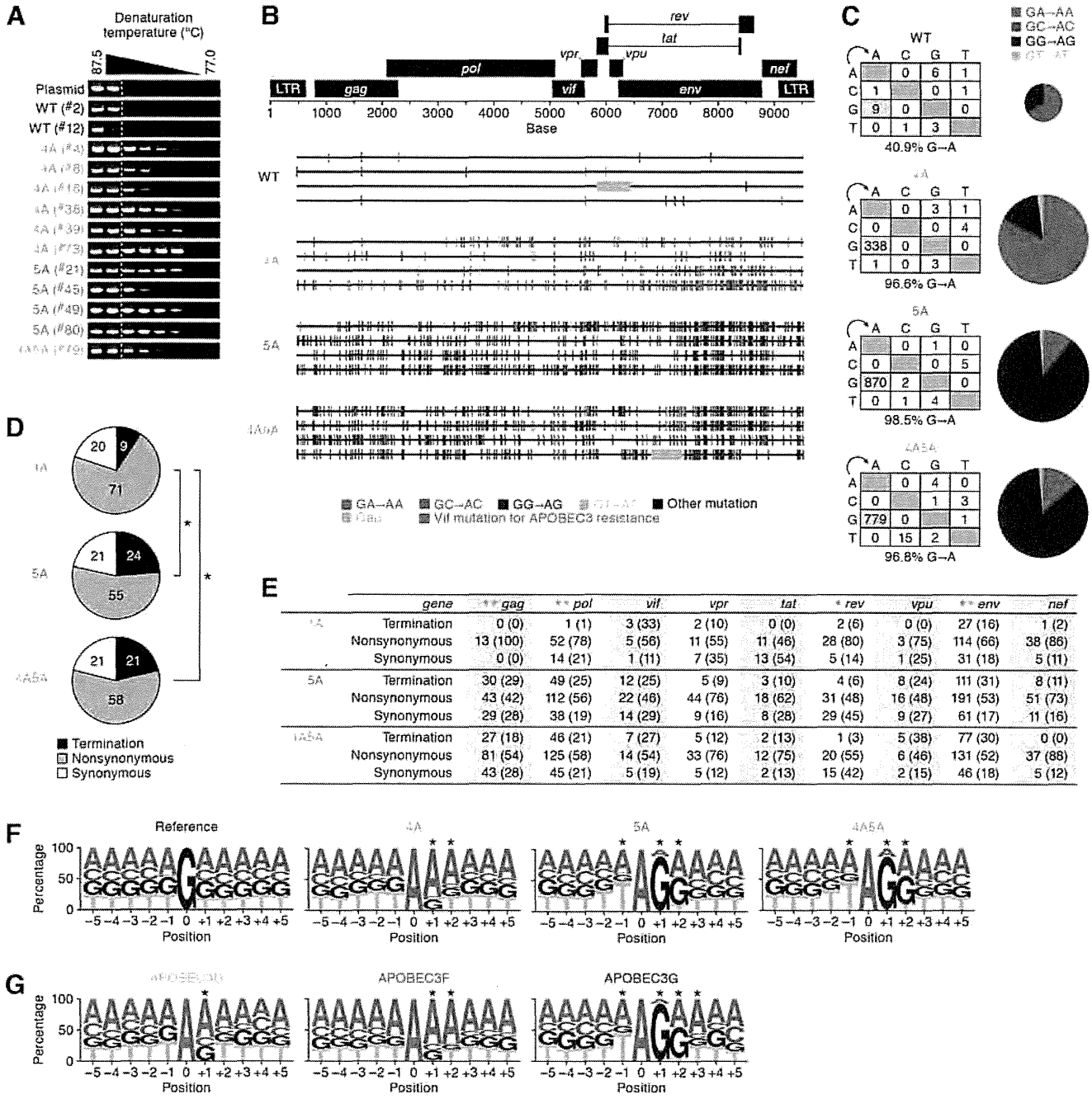

	gene	gag	pol	vif	vpr	tat	rev	vpu	env	nef
4A	Termination	0 (0)	1 (1)	3 (33)	2 (10)	0 (0)	2 (6)	0 (0)	27 (16)	1 (2)
	Nonsynonymous	13 (100)	52 (78)	5 (56)	11 (55)	11 (46)	28 (80)	3 (75)	114 (66)	38 (86)
	Synonymous	0 (0)	14 (21)	1 (11)	7 (35)	13 (54)	5 (14)	1 (25)	31 (18)	5 (11)
5A	Termination	30 (29)	49 (25)	12 (25)	5 (9)	3 (10)	4 (6)	8 (24)	111 (31)	8 (11)
	Nonsynonymous	43 (42)	112 (56)	22 (46)	44 (76)	18 (62)	31 (48)	16 (48)	191 (53)	51 (73)
	Synonymous	29 (28)	38 (19)	14 (29)	9 (16)	8 (28)	29 (45)	9 (27)	61 (17)	11 (16)
4A5A	Termination	27 (18)	46 (21)	7 (27)	5 (12)	2 (13)	1 (3)	5 (38)	77 (30)	0 (0)
	Nonsynonymous	81 (54)	125 (58)	14 (54)	33 (76)	12 (75)	20 (55)	6 (46)	131 (52)	37 (88)
	Synonymous	43 (28)	45 (21)	5 (19)	5 (12)	2 (13)	15 (42)	2 (15)	46 (18)	5 (12)

Figure 4. G-to-A hypermutation in the proviral DNA of infected humanized mice. (A) Semiquantitative 3D-PCR. Representative results are shown. Mouse IDs are shown in parentheses (correspond to those in Table S2). The dotted line indicates the lowest denaturation temperature (86.8°C) at which the PCR product is amplified from WT HIV-1-infected mice (mouse ID #2). (B and C) Full-length proviral DNA were cloned and sequenced as described in Materials and Methods. Representative results (B), mutation matrix (C, *left*), and pie chart of G-to-A mutation (C, *right*) are respectively shown. The diameters of pie charts represent the percentage of G-to-A mutations in total mutations. (D and E) Effect of G-to-A mutation in proviral DNA. (D) Pie chart of the effect of G-to-A mutation in full-length proviral DNA. The numbers in pie chart represent the percentage of termination, nonsynonymous, and synonymous mutations in G-to-A mutations, respectively. (E) Summary of the effect of G-to-A mutation in proviral DNA. The numbers and the percentages (in parentheses) of termination, nonsynonymous, and synonymous G-to-A mutations in each viral gene are summarized. Asterisks represent statistically significant differences ($P<0.01$ by Chi-square test for independence). In panel E, each color of asterisk represents the statistically significant difference between 4A HIV-1 and each HIV-1 *vif* mutant. (F and G) G-to-A mutation sites in the proviral DNA of infected mice (F) and *in vitro* infection assay (G) were respectively classified according to the nucleotides positioned between −5 to +5 from the detected G-to-A mutation sites (position 0). The results were respectively compared to that expected if G-to-A mutations occurred randomly occurred (F, 'reference'). *$P<0.001$ between the obtained and the expected results in each position by Chi-square test for independence. See also Figure S5.
doi:10.1371/journal.ppat.1004453.g004

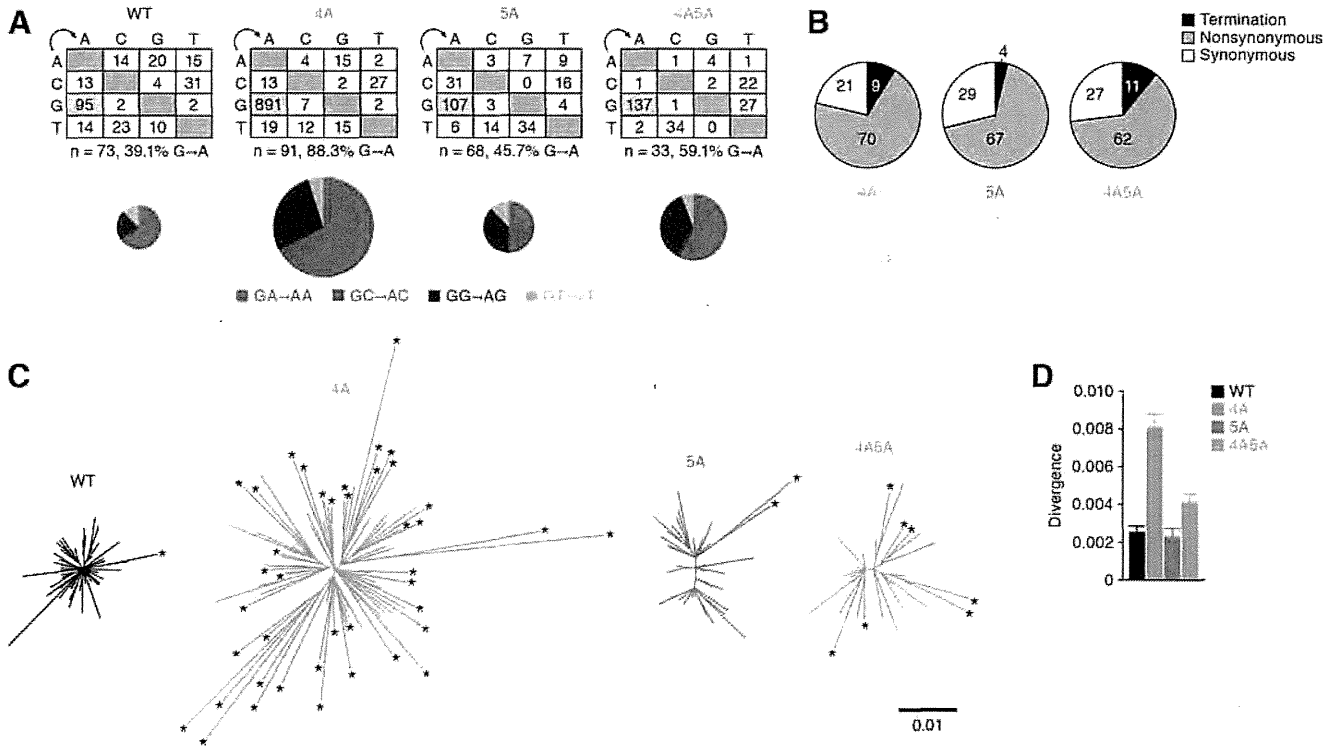

Figure 5. Diversification and functional evolution of 4A HIV-1 *in vivo*. The *env* ORFs (6221–8782, 2,562 bases) of viral RNA in the plasma of infected mice (WT, n = 73 from 2 mice; 4A, n = 91 from 3 mice; 5A, n = 68 from 2 mice; and 4A5A, n = 33 from 1 mouse) were sequenced by SGS assay. Raw data are shown in Figure S7. (A) The mutation matrix (*top*) and the pie chart of G-to-A mutation (*bottom*) are shown. In the bottom panel, the diameters of pie charts represent the percentage of G-to-A mutations in total mutations. (B) Effect of G-to-A mutation in *env* ORF of viral RNA in plasma. Pie chart of the effect of G-to-A mutation in *env* ORF is shown. The numbers in pie chart represent the percentage of termination, nonsynonymous, and synonymous mutations in G-to-A mutations, respectively. (C and D) Divergence of viral RNA sequence. Phylogenic trees (C) and genetic diversity (D) of *env* ORF sequences in the plasma of infected mice are shown. In panel C, the scale bar indicates the number of substitutions per site. The amplicons harboring statistically significant levels of G-to-A mutations ($P<0.05$ by Fisher's exact test using Hypermut 2.0) are indicated by asterisks.

doi:10.1371/journal.ppat.1004453.g005

rarely detected in WT, 5A, and 4A5A HIV-1-infected mice (Figure S8). Moreover, although termination mutations were prominently detected in the proviral DNA of 5A and 4A5A HIV-1-infected mice (Figures 4D and 4E), the percentages of termination mutation in the viral RNA in plasma of 5A and 4A5A HIV-1-infected mice were comparable to that of 4A HIV-1-infected mice (Figure 5B; 4A HIV-1 versus 5A HIV-1, $P = 0.06$; 4A HIV-1 versus 4A5A HIV-1, $P = 0.19$ by Chi-square test for independence). These findings strongly suggest that APOBEC3G-mediated G-to-A mutations frequently result in lethal mutations.

Interestingly, the phylogenic trees displayed that the *env* sequences in 4A HIV-1-infected mice were highly divergent and harbored significant levels of G-to-A mutations (Figure 5C). Furthermore, the analyses on genetic distance directly demonstrated that the *env* RNA sequences of 4A HIV-1-infected mice were highly divergent when compared to those of WT, 5A, and 4A5A HIV-1-infected mice (Figure 5D). Taken together, these findings provide strong evidence that APOBEC3F and APOBEC3D have the potential to restrict HIV-1 propagation, but at the same time, can also augment the emergence of quasispecies through sub-lethal G-to-A mutations *in vivo*.

Emergence of CCR5/CXCR4 dual-tropic HIV-1 in 4A HIV-1-infected mice

As shown in Figure 6A, mutations were detected in both conserved and variable regions of *env*. Previous studies have demonstrated that the variable region 3 (V3) of *env*, particularly the residues positioned at 11 and 25 in the V3, determines the CCR5 or CXCR4 coreceptor usage for HIV-1 entry [52,53]. Since we detected the diversified *env* sequences particularly in 4A HIV-1-infected mice (Figure 5C), we hypothesized the emergence of viruses that can use CXCR4 as the coreceptor in 4A HIV-1-infected mice. To address this possibility, we screened putative CXCR4-tropic HIV-1 by using a geno2pheno tool, which predicts the coreceptor usage based on nucleotide sequence [54], and found that the frequency of putative CXCR4-tropic HIV-1 in 4A HIV-1-infected mice was significantly higher than those in mice infected with WT, 5A, and 4A5A HIV-1s (Figure 6B, *left*). The detected putative CXCR4-tropic viruses were a N7S mutant from a WT HIV-1-infected mouse, a G24R mutant from a 4A HIV-1-infected mouse, and five E25K mutants from three 4A HIV-1-infected and one 4A5A HIV-1-infected mice (Figure 6B, *right*). It was particularly noteworthy that the E25K mutant detected was due to GAA-to-AAA mutation, which is the mutation signature mediated by APOBEC3F and APOBEC3D. To functionally evaluate whether these mutants can use CXCR4 as the coreceptor, we prepared the mutated virus based on NLCSFV3, which exclusively use CCR5 as the coreceptor. As shown in Figure 6C, we directly demonstrated that the infectivity of E25K mutant in $CXCR4^+$ MaRBLE cells was 2.5-fold higher than that of parental NLCSFV3 with a statistical significance ($P = 0.0073$). Taken together, these findings strongly suggest that the G-to-A

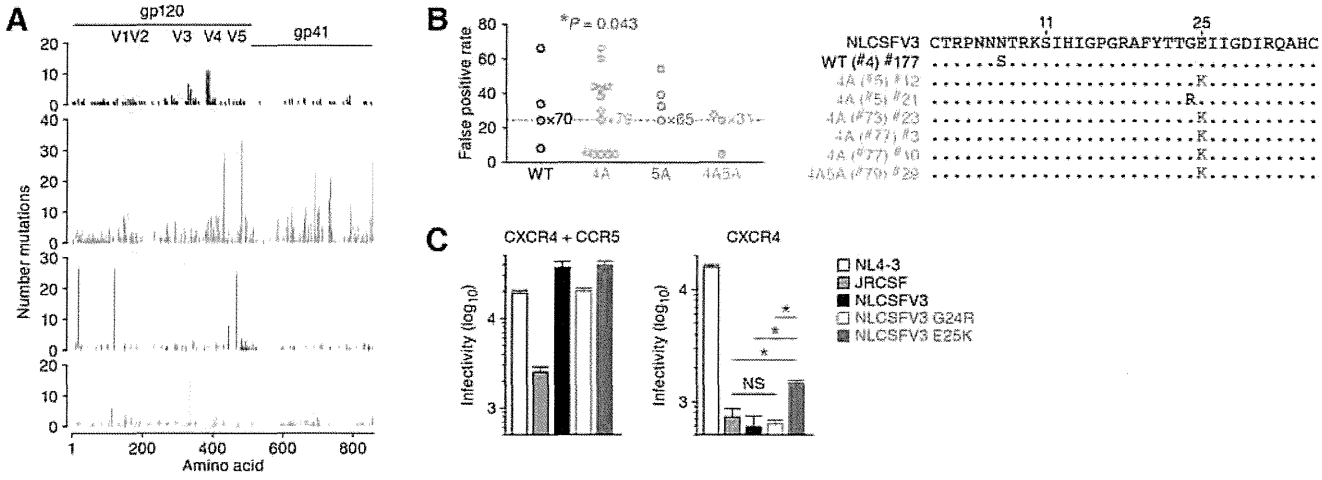

Figure 6. Functional evolution of 4A HIV-1 *in vivo*. (A) Mutations in *env* ORFs. (B) Estimation of coreceptor usage. Putative coreceptor usage was determined by using a geno2pheno coreceptor algorithm [54] as described in Materials and Methods. Mouse IDs are shown in parentheses (correspond to those in Table S2). The frequency of putative CXCR4-tropic HIV-1 in 4A HIV-1-infected mice was significantly higher than those in the mice infected with the other viruses ($P = 0.043$ by Chi-square test for independence). (C) Functional evaluation of coreceptor usage. Viral infectivity was measured by MaRBLE assay using R5-MaRBLE cells (*left*) and X4-MaRBLE cells (*right*). The data represents average with SD. The assay was performed in triplicate. Asterisks represent statistically significant differences ($P<0.05$ by Student's *t* test). NS, no statistical significance.
doi:10.1371/journal.ppat.1004453.g006

mutation mediated by APOBEC3F and APOBEC3D can contribute to the conversion of viral coreceptor usage from CCR5 to CXCR4.

Discussion

Previous studies including ours have demonstrated that endogenous APOBEC3 proteins have robust potential to diminish HIV-1 replication in humanized mouse models [23,41]. Furthermore, Krisko et al. have demonstrated that greater than 80% of G-to-A mutations in their *in vivo* experiments were in the context of GG-to-AG mutations, suggesting that endogenous APOBEC3G is the dominant restricting factor *in vivo* [41]. However, there are no reports that directly evaluate and compare the sole effects of endogenous APOBEC3G and/or APOBEC3D/F on HIV-1 replication *in vivo*. In addition, these papers [23,41] did not explore the possibility that endogenous APOBEC3 protein(s) may contribute to viral diversification. In our present study, we directly examined these two issues by using 3 kinds of HIV-1 *vif* mutants and a humanized mouse model. We demonstrated that endogenous APOBEC3G and APOBEC3D/F are intrinsic restriction factors against HIV-1. Moreover, we observed that endogenous APOBEC3D and APOBEC3F are capable of enhancing viral diversification *in vivo*.

We found that the propagation of HIV-1 *vif* mutants, particularly 5A and 4A5A, was severely suppressed even at high doses (Figures 2A–2D and S2). Consistent with previous reports [42,43], endogenous *APOBEC3G* was highly expressed in the splenic human $CD4^+$ T cells of humanized mice when compared to *APOBEC3F* and *APOBEC3D* (Figure 3B). In addition, the proviral DNA of 5A and 4A5A HIV-1-infected mice exhibited TGGG-to-TAGG hypermutations (Figure 4F), and APOBEC3G preferentially targeted to the tetranucleotide TGGG as substrate (Figure 4G), which readily results in termination codon mutations (Figures 4D and 4E). These findings indicate that endogenous APOBEC3G is an intrinsic factor that severely restricts HIV-1 propagation *in vivo*.

It was notable that the proviral DNA (Figures 4B–4F) and the *vif* ORF in the spleens of 4A5A HIV-1-infected mice (Figure S3) exhibited the signature of APOBEC3G-mediated mutations. In this regard, an *in silico* study has been recently reported that APOBEC3G and APOBEC3F rarely co-mutate the same viral genome in infected individuals [55]. Because the expression level of *APOBEC3G* was higher than those of *APOBEC3F* and *APOBEC3D* (Figure 3B), our findings suggest that APOBEC3G more predominantly affects HIV-1 replication *in vivo* than APOBEC3F and APOBEC3D.

When compared to APOBEC3G, the potential role of APOBEC3D and APOBEC3F in inhibition of viral replication has been controversial. Refsland and colleagues have recently demonstrated the anti-HIV-1 ability of APOBEC3D and APOBEC3F endogenously expressed in a human $CD4^+$ T cell line called CEM2n cells [15]. On the other hand, certain previous studies using human PBMC *in vitro* cultures have suggested that endogenously expressed APOBEC3F moderately restricts [56] or does not restrict [16] *vif*-deficient HIV-1 replication. In this regard, it should be noted that *in vitro* culture conditions use human $CD4^+$ T cell lines and/or human PBMCs artificially activated with mitogens such as phytohemagglutinin, which may not exactly mimic *in vivo* conditions, and therefore, may not reproduce the expression levels of APOBEC3D and APOBEC3F *in vivo*. Thus, it was important to carry out the *in vivo* experiments, which now firmly establish that APOBEC3D/F do indeed exert a substantial anti-viral effect on HIV-1 replication (Figures 2A–2D).

Although we demonstrated that the growth kinetics of 4A HIV-1 was significantly impaired compared to WT HIV-1 (Figures 2A–2D), the kinetics of 4A HIV-1 varied in each mouse (Figure 3A) and were significantly higher than those of 5A and 4A5A HIV-1 (Figures 2C and 2D). Also, the growth kinetics of 4A HIV-1 significantly and negatively correlated to the expression level of *APOBEC3F* but not *APOBEC3D* (Figure 3D), suggesting that endogenous APOBEC3F more critically modulates 4A HIV-1 replication *in vivo* than APOBEC3D. In fact, endogenous expression level of *APOBEC3F* was higher than that of *APOBEC3D* (Figure 3B). Moreover, anti-HIV-1 activity of APOBEC3F was higher than that of APOBEC3D in *in vitro*

transfection experiments (Figures 1C and S1), which are consistent with previous reports [13,17,48]. Therefore, these results suggest that the growth kinetics of 4A HIV-1 is predominantly impaired by APOBEC3F rather than APOBEC3D.

It is known that certain APOBEC3 proteins can impair HIV-1 replication by inhibiting viral reverse transcription (RT) independently of their deaminase activities [57–60]. In this regard, based on an experimental-mathematical approach, we have recently demonstrated that APOBEC3G restricts HIV-1 replication almost completely in a deaminase activity-dependent manner, while APOBEC3F impairs viral replication with the combination of G-to-A mutations and inhibition of viral RT [61]. In addition, although a deaminase-defective APOBEC3G mutant (E259Q) severely lost its anti-viral effect by 173-fold, the anti-viral effect of the deaminase-defective APOBEC3D (E264Q) and APOBEC3F (E251Q) differed only 2–3-fold compared to the WT proteins (Figure S1). These findings suggest that the anti-viral effect of APOBEC3D and APOBEC3F may be partially attributed to their deaminase-independent properties. On the other hand, Albin et al. have recently reported that *vif*-deficient HIV-1 can overcome the anti-viral effect of deaminase-defective APOBEC3F in a spreading infection experiment using T cell lines, and that APOBEC3F's deaminase activity is crucial for long-term restriction of *vif*-deficient HIV-1 replication [62]. Moreover, Mbisa et al. previously reported that virion-incorporated APOBEC3F and APOBEC3G potently inhibit HIV-1 integration [63]. Thus, these findings indicate that APOBEC3 proteins potently suppress HIV-1 replication by at least 3 different modes: (i) G-to-A mutation; (ii) inhibition of viral RT; and (iii) inhibition of viral integration; moreover, the magnitude of each mode of inhibition may be different for specific APOBEC3 proteins. Because APOBEC3's anti-viral modes are complex and intertwined, it would be technically impossible to quantitatively elucidate this under *in vivo* conditions. However, when compared to the mutation signature of APOBEC3G (T*G*GG-to-T*A*GG), APOBEC3D and APOBEC3F respectively preferred the dinucleotide (*G*A) and trinucleotide (*G*AA), which rarely led to stop codon mutations (Figure 4G) [61]. Although the extent of deaminase-dependent anti-HIV-1 activity of APOBEC3 proteins *in vivo* remains undetermined, our results suggest that endogenous APOBEC3D and APOBEC3F may inhibit HIV-1 replication *in vivo* in a manner that is less dependent on their deaminase activity than APOBEC3G.

Separate from the anti-HIV-1 ability of APOBEC3 proteins, some papers have suggested that the mutations generated by APOBEC3 proteins, particularly APOBEC3G, can promote viral evolution [18,19,21]. In this regard, it was particularly noteworthy that the viral RNA sequences in the plasma of 4A HIV-1-infected mice were highly diversified when compared to those of WT, 5A, and 4A5A HIV-1-infected mice (Figures 5C and 5D). These findings suggest that the G-to-A mutations mediated by APOBEC3D and APOBEC3F, but not by APOBEC3G, can increase the genetic diversity of viral populations. In fact, here we directly showed the emergence of CCR5/CXCR4 dual-tropic HIV-1 most exclusively in 4A HIV-1-infected mice (4 out of the 91 amplicons analyzed; Figure 6C, *right*), and the 4 E25K amplicons detected had intact ORFs (i.e., no termination mutations in the amplicon). More importantly, the E25K mutant in the V3 region of *env*, a coreceptor-switched HIV-1, was generated by a *G*AA-to-*A*AA mutation, strongly suggesting that this mutation may be caused by APOBEC3F, and also possibly APOBEC3D. Regarding viral coreceptor usage, it is well known that the charge of two specific amino acids in the V3 region of HIV-1 Env, positioned at 11 and 25, strongly influence the coreceptor usage [52,53]. Our findings strongly suggest that one of the two crucial mutations, E25K, needed for conversion of CCR5 to CXCR4 usage, is facilitated by APOBEC3D/F. This makes it more likely that coreceptor conversion will occur as a result of a random RT error leading to a substitution at the position 11 in genomes that have the APOBEC3D/F-associated mutation.

In addition to the conversion of coreceptor usage (Figure 6C), we found that the sites preferred by APOBEC3D and APOBEC3F may potentially lead to the resistance to anti-HIV-1 drugs (Table S1). Furthermore, our results suggest that 4A HIV-1 can propagate *in vivo* when APOBEC3F expression level was relatively low (Figure 3D). Our data further suggest that sub-lethal G-to-A mutations caused by endogenous APOBEC3D and APOBEC3F, which are expressed at a lower level, rather than APOBEC3G, can lead to diversification of HIV-1 genomes leading to increased viral variation and evolutionary potential. Although our viruses used in this study produce defective Vifs, we believe it reflects the natural infection because Simon et al. have shown that defective *vif*s are often seen during natural infection in patients [64]. Thus, the types of mutations and diversification we observed in this study would be quantitatively higher, but similar to the diversification that occurs during natural infection, as a result of the emergence of *vif*-mutated viruses.

In conclusion, here we demonstrated that endogenous APOBEC3G is the *bona fide* anti-HIV-1 restriction factor even *in vivo*. On the other hand, we also provide strong evidence indicating that endogenous APOBEC3D and APOBEC3F suppress viral replication *in vivo*, while these proteins potently induce viral evolution. These findings suggest that the impairment of Vif-APOBEC3G interaction can be a novel target for anti-HIV-1 drugs, while the restoration of deaminase activity of APOBEC3D and APOBEC3F by inhibiting Vif-mediated degradation may potentially lead to the enhancement of viral diversification. As shown in Figure 1B, both DRMR and YRHHY motifs are exposed on the surface of Vif protein [39]. Therefore, it may be possible to design compounds that target the YRHHY motif and specifically block Vif-APOBEC3G interaction, which may be ideal candidates for development of novel anti-HIV-1 drugs.

Materials and Methods

Ethics statement

All procedures including animal studies were conducted following the guidelines for the Care and Use of Laboratory Animals of the Ministry of Education, Culture, Sports, Science and Technology, Japan. The authors received approval from the Institutional Animal Care and Use Committees (IACUC)/ethics committee of Kyoto University institutional review board (protocol number D13-25). All protocols involving human subjects were reviewed and approved by the Kyoto University institutional review board. Informed written consent from human subjects was obtained in this study.

Humanized mice

NOG mice [65] were obtained from the Central Institute for Experimental Animals (Kawasaki, Kanagawa, Japan). The mice were maintained under specific-pathogen-free conditions and were handled in accordance with the regulation of IACUC/ethics committee of Kyoto University. Human $CD34^+$ hematopoietic stem cells were isolated from human fetal liver as previously described [66]. The humanized mouse (NOG-hCD34 mouse) was constructed as previously described [22–27]. Briefly, 82 newborn (aged 0 to 2 days) NOG mice from 19 litters were irradiated with X-ray (10 cGy per mouse) by an RX-650 X-ray cabinet system

(Faxitron X-ray Corporation) and were then intrahepatically injected with the obtained human fetal liver-derived $CD34^+$ cells (8×10^4 to 17×10^4 cells). A list of the humanized mice used in this study is summarized in Table S2.

Cell culture

293T cells and TZM-bl cells (obtained through the NIH AIDS Research and Reference Reagent program) [67] were maintained in DMEM containing 10% fetal calf serum (FCS) and antibiotics. X4-MaRBLE and R5-MaRBLE cells (kindly provided by Dr. Wataru Sugiura) [68] were maintained in RPMI 1640 containing 10% FCS and antibiotics. For X4-MaRBLE cells, 250 μg/ml Geneticin and 0.1 μg/ml Puromycin were added to the culture medium. For R5-MaRBLE cells, 150 μg/ml Hygromycin B, 250 μg/ml Geneticin, and 0.1 μg/ml Puromycin were added to the culture medium.

Virus preparation and infection

IMCs of CCR5-tropic HIV-1 (strain NLCSFV3) [40] and its derivatives were constructed based on pNLCSFV3 [40]. To construct pNLCSFV3-DRMR/AAAA (pNLCSFV3-4A), pNLCSFV3-YRHHY/AAAAA (pNLCSFV3-5A), and pNLCSFV3*Δvif*, the *Age*I-*Eco*RI fragments of pNL4-3-based these mutants [17,38,69] and pNL4-3*Δvif* [70] were subcloned into the *Age*I-*Eco*RI site of pNLCSFV3 [40]. To construct pNLCSFV3-4A5A, the 5A mutation was inserted into pNLCSFV3-4A as previously described [69]. The sequences of these constructed plasmids were confirmed by sequencing PCR. To prepare the virus solutions for the experiments using humanized mice, 30 μg of pNLCSFV3 or its derivatives (pNLCSFV3-4A, pNLCSFV3-5A, or pNLCSFV3-4A5A) was transfected into 293T cells by the calcium-phosphate method as previously described [23,25]. After 48 h posttransfection, the culture supernatant was harvested, centrifuged, and then filtrated through a 0.45-μm filter (Millipore) to produce virus solution. The amount of virus particles was quantified by using an HIV-1 p24 antigen ELISA kit (Zeptometrix), and 50% infectious dose (ID_{50}) was measured by Reed-Meunch's method as previously described [25]. Virus solutions containing 5 ng (Figure 2), 50 ng and 500 ng (Figure S2) of p24 antigen (equivalent to 1,500, 15,000, and 150,000 ID_{50}, respectively) were intraperitoneally inoculated into NOG-hCD34 mice. RPMI 1640 was used for mock infection.

Peripheral blood collection, mononuclear cell isolation, and quantification of HIV-1 RNA in plasma

Peripheral blood and plasma were collected at 0, 1, 2, 3, 5, and 6 wpi as previously described [22,23,25,26]. The mice were sacrificed at 6 wpi with anesthesia, and the spleen was crushed, rubbed, and suspended as previously described [22,23,25,26]. To obtain splenic human MNCs, the splenic cell suspension was separated by using Ficoll-Paque (Pharmacia) as previously described [22,23,25,26]. The amount of HIV-1 RNA in 50 μl plasma was quantified by Bio Medical Laboratories, Inc. (the detection limit of HIV-1 RNA is 800 copies/ml).

Flow cytometry and hematometry

Flow cytometry was performed with a FACS Canto II (BD biosciences) as previously described [22,23,25,26], and the obtained data were analyzed with Cell Quest software (BD biosciences) and FlowJo software (Tree Star, Inc.). For flow cytometry analysis, anti-CD45-PE (HI30; Biolegend), anti-CD3-APC-Cy7 (HIT3a; Biolegend), and anti-CD4-APC (RPA-T4; Biolegend) antibodies were used. Hematometry was performed with a Celltac α MEK-6450 (Nihon kohden, Co.) as previously described [23,25,26].

Transfection, western blotting, TZM-bl assay, and MaRBLE assay

In vitro transfection experiments were performed by using Lipofectamine 2000 (Life technologies) according to the manufacture's protocol. After 48 h posttransfection, the culture supernatant was harvested, centrifuged, and then filtrated through a 0.45-μm filter (Millipore) to produce virus solution. For the experiments shown in Figure 1C, 2 μg of pNLCSFV3 or its derivatives (pNLCSFV3-4A, pNLCSFV3-5A, or pNLCSFV3-4A5A) was cotransfected with 100 ng of flag-tagged APOBEC3D, APOBEC3F, or APOBEC3G expression plasmid into 293T cells. For the experiments shown in Figures 2E and 2F, 500 ng of pNLCSFV3*Δvif* and 500 ng of Vif expression plasmids (see below) were cotransfected with 50 ng of flag-tagged APOBEC3F or APOBEC3G expression plasmid [17] into 293T cells. For the experiments shown in Figure 4G, 2 μg of pNLCSFV3*Δvif* was cotransfected with 100 μg of flag-tagged APOBEC3D, APOBEC3F, or APOBEC3G expression plasmid into 293T cells. The virus solutions were prepared as described above. Then, the virus solutions were treated with DNase I (50 unit; Takara) at 37°C for 1 h and inoculated into TZM-bl cells. The infected TZM-bl cells were harvested at 18 h postinfection and DNA was extracted as described below. Western blotting was performed as previously described [23,25], and anti-Vif antibody (clone #2221; obtained through the NIH AIDS Research and Reference Reagent program) and anti-α-Tubulin (TUBA) monoclonal antibody (DM1A; Sigma) were used. To quantify the infectivity of virus solution, TZM-bl assay was performed as previously described [23,25]. MaRBLE assay was performed as previously described [68] with minor modifications. Briefly, the virus solutions (normalized to the amount of p24 antigen) were inoculated into X4-MaRBLE or R5-MaRBLE cells (1×10^5 cells). At 72 h postinfection, the cells were harvested, and the luciferase activity was measured as previously described [71].

PCR, RT-PCR, and real-time RT-PCR

DNA and RNA were extracted from the splenic human MNCs at 6 wpi or infected TZM-bl cells as previously described [23,25]. cDNA was prepared by using SuperScript III reverse transcriptase (Life technologies) with DNase I (Life technologies), RNaseOUT (Life technologies), and random primers according to the manufacture's procedure. To amplify *vif* ORF (Figures 2E, 2F, and S3), RT-PCR was performed by using PrimeSTAR GXL DNA polymerase (Takara) according to the manufacture's protocol, and the following primers were used: Vif-fwd (4929–4948), 5′-gtt tgg aaa gga cca gca aa-3′; and Vif-rev (5703–5722), 5′-gcc caa gta tcc ccg taa gt-3′. To analyze the sequence of full-length proviral DNA (Figures 4B–4E and S6), PCR was performed by using *Pfu* Ultra II DNA polymerase (Stratagene) according to the manufacture's protocol, and the following primers were used: 5′ region (475–1698, 1,224 bp), 5LTRF#1 (455–474), 5′-ggt ctc tct ggt tag acc ag-3′; and 5LTRR#1 (1699–1718), 5′-gaa gct tgc tcg gct ctt ag-3′; 5′/central region (1342–3530, 2,189 bp), 5F#7 (1322–1341), 5′-gag cca ccc cac aag att ta-3′; and 5/cR#7 (3531–3550), 5′-tgc ccc tgc ttc tgt att tc-3′; central/3′ region (3420–5888, 2,469 bp), C#3F (3400–3419), 5′-ggg gaa cca aag cac taa ca-3′; and 5R#1 (5889–5913), 5′-ttt aca ata gca att ggt aca agc a-3′; 3′ region (5453–9526, 4,074 bp), 3F#2 (5428–5452), 5′-agt cct agg tgt gaa tat caa gca g-3′; and 3LTRR#1 (9527–9547), 5′-ctg gtc taa cca gag aga cc-3′. The products of PCR and RT-PCR were cloned into pCRII-blunt-TOPO by using Zero

blunt TOPO PCR cloning kit (Life technologies) according to the manufacture's protocol. To prepare the expression plasmids of the Vif mutants (Figures 2E and 2F), the pCRII-blunt-TOPO containing *vif* ORFs were digested with *EcoR*I and blunted. The obtained DNA fragments containing *vif* ORF were subcloned into the *Hpa*I site of pDON-AI (Takara). Real-time RT-PCR was performed as previously described [23]. Briefly, *APOBEC3D, APOBEC3F, APOBEC3G* [43] and *IFNB* [72] were amplified by using the primers previously reported. The primers for *GAPDH* were purchased from Life technologies. The expression levels of *APOBEC3D, APOBEC3F*, and *APOBEC3G* (Figure 3C) were standardized as previously described [42,43]. To construct pNLCSFV3 G24R and E25K (Figure 6C), the DNA sequences containing *env* G24R or E25K mutations were digested with *Mlu*I and *Xba*I, and the resultant DNA fragments were subcloned into the *Mlu*I-*Xba*I site of pNLCSFV3.

SGS assay

SGS assay was performed as previously described [50]. Briefly, viral RNA was extracted from the plasma (100 μl) of infected mice at 6 wpi by using QIAamp viral RNA mini kit (Qiagen), and cDNA was prepared as previously described [50].

Sequencing PCR

Sequencing PCR was performed as previously described [23], and the sequence data were analyzed by Seqscape software v2.5 (Applied Biosystems) and Sequencher software (Hitachi). To analyze the sequence of *vif* (Figures 2E, 2F and S3), M13 primers were used. To analyze the sequence of full-length proviral DNA (Figures 4B–4G and S6), M13 primers and the following primers were used: 5#6 (1609–1633), 5′-gta aga atg tat agc cct acc agc a-3′; Cl#1 (2178–2197), 5′-cag gtt tgg gga aga gac aa-3′; C#2 (2700–2719), 5′-ggg cct gaa aat cca tac aa-3′; C#4 (4004–4023), 5′-ttt gca gga ttc ggg att ag-3′; C#5 (4499–4518), 5′-agc aga gac agg gca aga aa-3′; C#6 (5058–5077), 5′-ggt gat gat tgt gtg gca ag-3′; 3#1 (5960–5979), 5′-gca tct cct atg gca gga ag-3′; 3#2 (6651–6660), 5′-gcg gga gaa tga taa tgg ag-3′; 3#3 (7315–7334), 5′-ccc aga aat tgt aac gca ca-3′; 3#4 (7947–7966), 5′-gaa tcc tgg ctg tgg aaa ga-3′; 3#5 (8511–8530), 5′-gct acc acc gct tga gag ac-3′; and 3#6 (8969–8988), 5′-gga gga aga ggt ggg ttt tc-3′. For SGS assay (Figure 5), direct sequencing was performed by using the primers used in the 2nd SGS PCR and the primers 3#2 and 3#3.

Semiquantitative 3D-PCR

Semiquantitative 3D-PCR (Figure 4A) was performed as previously described [48]. Briefly, we used the following primers according to the previous report [48]: 1st-fwd (2723–2746), 5′-tcc art att trc cat aaa raa aaa-3′; 1st-rev (3575–3598), 5′-tty aga ttt tta aat ggy tyt tga-3′; 2nd-fwd (3023–3049), 5′-aat att cca rtr tar cat rac aaa aat-3′; and 2nd-rev (3561–3586), 5′-aat ggy tyt tga taa att tga tat gt-3′. The 1st PCR products were quantified, and constant amounts were used for secondary PCR over 87.5 to 77.0°C range of denaturation temperatures. The 2nd PCR products were run on agarose gels and were visualized by staining with ethidium bromide.

Sequence data analysis and bioinformatics

To analyze the diversity of *vif* in HIV-1 group M (Figure 1A), we obtained 7,118 *vif* ORF sequences registered in Los Alamos HIV sequence database (http://www.hiv.lanl.gov). The 7,118 datasets were aligned by using ClustalW [73] implemented in MEGA 5.1 software [74], and the logo plot shown in Figure 1A was generated by using WebLogo 3 (http://weblogo.threeplusone.com/). To analyze the effect of G-to-A mutation in proviral DNA (Figures 4D and 4E), the sequences of all viral genes (*gag, pol, vif, vpr, tat, rev, vpu, env, and nef*) were obtained from the sequence of full-length proviral DNA (Figure 4B), and the codon-based alignments were constructed using a Gene Cutter tool from the Los Alamos HIV sequence database (http://www.hiv.lanl.gov/content/sequence/GENE_CUTTER/cutter.html). The effect of G-to-A mutation in *env* ORF of viral RNA (Figure 5B) was also analyzed as descried above. To analyze APOBEC3-mediated mutations (Figures 4F and 4G), hypermut 2.0 (http://www.hiv.lanl.gov/content/sequence/HYPERMUT/hypermut.html) was used. The *env* ORF sequences obtained by SGS (see above) were aligned by using ClustalW [73] implemented in MEGA 5.1 software [74]. The sequence of WT NLCSFV3 *env* was used as outgroup. The best fitting substitution model was determined using jModelTest 2.1.3. [75]. The Akaike information criterion (AIC) implemented in jmodeltest-2.1.3 selected GTR+I+G as the best-fit. Since this model is not available in MEGA 5.1 software, the TrN+I+G [76], the second best-fit model, was used in further analyses. Genetic distances among *env* ORF sequences (Figure 5D) were calculated with MEGA 5.1 software under the Tamura-Nei model [76]. ML phylogenetic trees (Figure 5C) were reconstructed using PhyML-3.1 under TN93 model [76] with 1,000 bootstrap resamplings [77]. The *env* V3 sequences determined by SGS were used for the genotypic coreceptor usage prediction based on an algorithm, geno2pheno coreceptor [54]. The original g2p coreceptor model was selected, and the sequences below the 10% false-positive rate cutoff were defined as putative CXCR4-tropic viruses (Figure 6B). The major drug resistance sites, which are potentially induced by APOBEC3D and APOBEC3F (Table S1), were determined based on the current IAS-USA lists [78]. The sequence of HIV-1 strain HXB2 (Genbank accession number: FB707281) were used as reference.

3D structure of Vif

The 3D structure of Vif (Figure 1B) was generated on PyMOL v1.6 (http://www.pymol.org/) with the crystal structure of Vif-CBFβ-CUL5-ELOB-ELOC complex (PDB code: 4N9F) [79].

Calculation of AUC of VL

The AUC (Figure 2C) was calculated from the VL data using the trapezoidal rule. For example, let us define that $V(t)$ is a VL at time t. Then the AUC from 0 to 6 wpi is calculated as follows:

$$\int_0^6 V(s)ds = \int_0^1 V(s)ds + \int_1^2 V(s)ds + \ldots + \int_5^6 V(s)ds \approx \sum_{w=1}^{6} \{w-(w-1)\}\frac{V(w-1)+V(w)}{2} = \sum_{w=1}^{6} \frac{V(w-1)+V(w)}{2}.$$

Estimation of virus replication rate

To quantify the dynamics during acute virus infection (Figure 2D), we used a recently developed model describing the loss of target cells phenomenologically as follows:

$$T(t) = T(0)\exp(\Delta_1 t), \text{ for } t < t*, \quad (1)$$

$$T(t) = T(0)\exp(\Delta_1 t*)\exp\{\Delta_2(t-t*)\}, \text{ for } t > t*, \quad (2)$$

$$\frac{dI(t)}{dt} = \beta T(t)V(t) - \delta I(t), \quad (3)$$

$$\frac{dV(t)}{dt} = pI(t) - cV(t). \quad (4)$$

Modeling HIV infection it is well accepted to make the quasi-steady assumption, $dV(t)/dt = 0$, and to write that $V(t) = p^*I(t)$, where p^* is a scaled production parameter ($p^* = p/c$). Because we are fitting VLs, $V(t)$, rather than number of infected cells, $I(t)$, we substitute $I(t) = V(t)/p^*$ into Eq. (3) to obtain

$$\frac{dV(t)}{dt} = \{r* T(t) - \delta\}V(t), \quad (5)$$

where $r^* = p^*\beta$ is the viral replication rate per target cell, and δ remains the death rate of infected cells. Because the number of target cells seems to decrease exponentially in phases during the acute phase of several virus infections, we approximated the dynamics of target cells by a piece-wise exponential function. The parameters Δ_1 and Δ_2 represent the two daily loss rates of target cells, and t^* represents the time at which the function switches slope. Because Eqs. (1), (2), and (5) define a non-autonomous linear differential equation, we derived the following analytical solution describing the acute phase of virus infections:

$$V(t) = V(0)\exp\left\{\frac{r* T(0)[\exp(\Delta_1 t) - 1]}{\Delta_1} - \delta(t)\right\}, \text{ for } t < t*, \quad (6)$$

$$V(t) = \quad (7)$$
$$V(t*)\exp\left\{\frac{r* T(t*)[\exp(\Delta_2(t-t*)) - 1]}{\Delta_2} - \delta(t-t*)\right\}, \text{ for } t > t*.$$

We employed the solution of Eqs. (1), (2), (6), and (7) to fit the 6-week time courses of VLs and target cells as shown in Figures 2 and S2 (using the FindMinimum package of *Mathematica 9.0* to minimize the sum of squared residuals). This model has 6 parameters: $T(0)$, Δ_1, Δ_2, $V(0)$, r^*, and δ. The first 3 parameters, $T(0)$, Δ_1, and Δ_2, are estimated from the observed number of peripheral $CD4^+$ T cells per ml of blood. For the latter 3 parameters, $V(0)$, r^*, and δ, we fix $\delta = 1$ per day [80,81], because this is general estimate for the death rate of productively infected cells. The initial value of VL, $V(0)$, was set to the detection limit of the assay (800 copies/ml plasma). The replication rate, r^*, was estimated from the data.

Statistical analysis

Data were presented as averages ± SEMs or SDs. Statistical differences were determined by Student's *t* test (Figures 1C, 2A–2D, 3C, and 6C), Chi-square test for independence (Figures 4D–4G, 5B, 6B, and S5), and Fisher's exact test (Figure 5C). To determine statistically significant correlation (Figures 3D and S4), Pearson correlation coefficient (r) was applied.

Accession numbers

The GenBank (http://www.ncbi.nlm.nih.gov/genbank/) accession numbers for the genes mentioned in the text are as follows: *APOBEC3D* (NM_152426), *APOBEC3F* (NM_145298), *APOBEC3G* (NM_021822), *IFNB* (NM_002176), and *GAPDH* (NM_002046).

Online supplemental material

Figure S1 shows the anti-viral activity of WT and catalytically inactive APOBEC3 proteins *in vitro*. Figure S2 shows the dynamics of WT HIV-1 and HIV-1 *vif* mutants infection in humanized mice at higher doses. Figure S3 shows the summary of mutations in *vif* ORF. Figure S4 shows the correlation of *APOBEC3* and *IFNB* expressions. Figure S5 shows the statistical analyses on the preferential G-to-A mutation sites. Figure S6 shows the summary of mutations in the proviral DNA of infected humanized mice. Figure S7 shows the raw data of SGS assay. Figure S8 shows the extent of mutation in each amplicon of viral *env*. Table S1 shows putative drug-resistance mutations potentially induced by APOBEC3D and APOBEC3F. Table S2 shows the list of humanized mice used in this study.

Supporting Information

Figure S1 Anti-viral activity of WT and mutated APOBEC3 proteins *in vitro*. Two micrograms of pNLCSFV3*Δvif* was cotransfected with 100 ng of flag-tagged APOBEC3 expression plasmid into 293T cells. (A) Western blotting. The input of cell lysate was standardized to α-Tubulin (TUBA), and representative results are shown. (B) TZM-bl assay. The infectivity of released virus was determined by using TZM-bl cells. The infectivity of each virus is normalized to the value of no APOBEC3. The assay was performed in triplicate. The data represents average with SD.
(TIF)

Figure S2 Dynamics of WT HIV-1 and HIV-1 *vif* mutants infection in humanized mice at higher doses. (A and B) Virus solutions containing 50 ng (A; 4A HIV-1 [n = 8], 5A HIV-1 [n = 8], and 4A5A HIV-1 [n = 6]) or 500 ng (B; 4A HIV-1 [n = 5], 5A HIV-1 [n = 8], and 4A5A HIV-1 [n = 6]) p24 antigens were intraperitoneally inoculated into humanized mice. The amount of viral RNA in plasma (*top*) and the level of peripheral $CD4^+$ T cells ($CD45^+$ $CD3^+$ $CD4^+$ cells) (*bottom*) were analyzed at 0, 1, 2, 3, 5, and 6 wpi. The averages are shown in circles with SEMs, and the values from each mouse are shown by line. In panel A, the detection limit of HIV-1 RNA is 800 copies/ml plasma.
(TIF)

Figure S3 Mutations in *vif* ORF. The *vif* ORFs (5041–5619, 579 bases) of viral RNA in the spleen of infected mice (WT, n = 82 from 3 mice; 4A, n = 320 from 7 mice; 5A, n = 132 from 3 mice; and 4A5A, n = 59 from 1 mouse) were sequenced. (A) The mutation matrix (*left*) and the pie chart of G-to-A mutation (*right*) are shown. In the *right* panel, the diameters of pie charts represent the percentage of G-to-A mutations in total mutations. (B) The extent of mutation in each amplicon of *vif* ORF sequences. The numbers of total mutations (*top*, gray), G-to-A mutations (*upper middle*, black), GA-to-AA mutations (*lower middle*, red), and GG-to-AG mutations (*bottom*, blue) within each amplicon are respectively shown. (C) The *vif* amplicons harboring nonsynonymous mutations are summarized. "X" means stop codon mutation. The *vif* ORFs indicated by asterisks were used for the functional assay, and the results are shown in Figures 2E and 2F. In the panel of 4A5A, the amplicon harboring both R132K and I124M mutations (indicated by double

daggers) were frequently detected and were used for the functional assay (Figures 2E and 2F).
(TIF)

Figure S4 Correlation of *APOBEC3* and *IFNB* expressions. The mRNA expression levels of *APOBEC3D*, *APOBEEC3F*, *APOBEC3G*, and *IFNB* in the splenic human $CD4^+$ T cells of humanize mice (n = 73) were measured by real-time RT-PCR. The expression level of each gene was normalized to that of *GAPDH* and was shown as relative expression. The correlation between each *APOBEC3* (A) and between *APOBEC3* (x-axes) and *IFNB* (y-axes) (B) are respectively shown. The lines represent exponential approximation. Pearson correlation coefficient (r) was adopted to determine statistically significant correlation between each value.
(TIF)

Figure S5 Statistical analyses on the preferential G-to-A mutation sites. The detected G-to-A mutation sites in the proviral DNA of *vif*-mutated HIV-1-infected mice (A) and *in vitro* experiments (B) were classified according to the nucleotides positioned between −5 to +5 from the detected G-to-A mutation sites (position 0; see also Figures 4F and 4G). Statistical differences at each position were determined by Chi-square test for independence, and the P values at each position is shown in y-axes. Statistically significant differences ($P<0.001$) are shown with asterisks.
(TIF)

Figure S6 Mutations in the proviral DNA of infected humanized mice. The percentages of mutations in each site are summarized.
(TIF)

Figure S7 Raw data of SGS assay. The *env* ORF (6221–8782, 2,562 bases) of viral RNA in the plasma of infected mice (WT, n = 73 from 2 mice; 4A, n = 91 from 3 mice; 5A, n = 68 from 2 mice; and 4A5A, n = 33 from 1 mouse) were analyzed by SGS assay, and the raw data are shown.
(TIF)

Figure S8 The extent of mutation in each amplicon of viral *env* in plasma. The numbers of total mutations (*top*, gray), G-to-A mutations (*upper middle*, black), GA-to-AA mutations (*lower middle*, red), and GG-to-AG mutations (*bottom*, blue) within each amplicon are respectively shown.
(TIF)

Table S1 Putative drug-resistance mutations potentially induced by APOBEC3D and APOBEC3F. The table provides the drug-resistance mutation sites potentially induced by APOBEC3D and APOBEC3F.
(PDF)

Table S2 Humanized mice used in this study. A full list of the 82 humanized mice used in this study.
(PDF)

Acknowledgments

We would like to thank Dr. John Coffin (Tufts University) for lively discussion and providing critical comments, Dr. Fengrong Ren (Tokyo Medical and Dental University) for supporting genetic distance analyses, Dr. Tobias Paprotka (NCI-Frederick, NIH) for helpful suggestion, Dr. Wataru Sugiura (National Hospital Organization Nagoya Medical Center) for providing experimental materials, Drs. Yoshinori Fukazawa (Oregon Health and Science University), Keiko Okano (Kyoto University Research Administration Office) and Seiga Ohmine (Mayo Clinic) for proofreading the manuscript, the colleagues belonging to iGEM Kyoto (Sakaya Aoki, Yoshitaka Hirano, Akiho Kojima, Yusuke Komoto, Mina Noura, Kenji Okumura, Toshiro Shimizu, Masako Terasaka, Moe Yanagi, and Mitsuaki Yoshida) for their experimental support, and Ms. Kotubu Misawa for the dedicated support.

Author Contributions

Conceived and designed the experiments: KS TI VKP YKo. Performed the experiments: KS JST NM TI TK YKi. Analyzed the data: KS JST NM TI TK YKi SI. Contributed reagents/materials/analysis tools: NM SI ATK WSH KA MI DSA. Wrote the paper: KS VKP YKo.

References

1. Conticello SG (2008) The AID/APOBEC family of nucleic acid mutators. Genome Biol 9: 229.
2. Conticello SG, Langlois MA, Yang Z, Neuberger MS (2007) DNA deamination in immunity: AID in the context of its APOBEC relatives. Adv Immunol 94: 37–73.
3. Teng B, Burant CF, Davidson NO (1993) Molecular cloning of an apolipoprotein B messenger RNA editing protein. Science 260: 1816–1819.
4. Harris RS, Liddament MT (2004) Retroviral restriction by APOBEC proteins. Nat Rev Immunol 4: 868–877.
5. Zhang J (2003) Evolution by gene duplication: an update. Trends Ecol Evol 18: 292–298.
6. Sawyer SL, Emerman M, Malik HS (2004) Ancient adaptive evolution of the primate antiviral DNA-editing enzyme APOBEC3G. PLoS Biol 2: E275.
7. Stenglein MD, Burns MB, Li M, Lengyel J, Harris RS (2010) APOBEC3 proteins mediate the clearance of foreign DNA from human cells. Nat Struct Mol Biol 17: 222–229.
8. Burns MB, Temiz NA, Harris RS (2013) Evidence for APOBEC3B mutagenesis in multiple human cancers. Nat Genet 45: 977–983.
9. Shinohara M, Io K, Shindo K, Matsui M, Sakamoto T, et al. (2012) APOBEC3B can impair genomic stability by inducing base substitutions in genomic DNA in human cells. Sci Rep 2: 806.
10. Burns MB, Lackey L, Carpenter MA, Rathore A, Land AM, et al. (2013) APOBEC3B is an enzymatic source of mutation in breast cancer. Nature 494: 366–370.
11. Sheehy AM, Gaddis NC, Choi JD, Malim MH (2002) Isolation of a human gene that inhibits HIV-1 infection and is suppressed by the viral Vif protein. Nature 418: 646–650.
12. Izumi T, Shirakawa K, Takaori-Kondo A (2008) Cytidine deaminases as a weapon against retroviruses and a new target for antiviral therapy. Mini Rev Med Chem 8: 231–238.
13. Dang Y, Wang X, Esselman WJ, Zheng YH (2006) Identification of APOBEC3DE as another antiretroviral factor from the human APOBEC family. J Virol 80: 10522–10533.
14. Liddament MT, Brown WL, Schumacher AJ, Harris RS (2004) APOBEC3F properties and hypermutation preferences indicate activity against HIV-1 *in vivo*. Curr Biol 14: 1385–1391.
15. Refsland EW, Hultquist JF, Harris RS (2012) Endogenous origins of HIV-1 G-to-A hypermutation and restriction in the nonpermissive T cell line CEM2n. PLoS Pathog 8: e1002800.
16. Miyagi E, Brown CR, Opi S, Khan M, Goila-Gaur R, et al. (2010) Stably expressed APOBEC3F has negligible antiviral activity. J Virol 84: 11067–11075.
17. Chaipan C, Smith JL, Hu WS, Pathak VK (2013) APOBEC3G restricts HIV-1 to a greater extent than APOBEC3F and APOBEC3DE in human primary $CD4^+$ T cells and macrophages. J Virol 87: 444–453.
18. Pillai SK, Wong JK, Barbour JD (2008) Turning up the volume on mutational pressure: is more of a good thing always better? (A case study of HIV-1 Vif and APOBEC3). Retrovirology 5: 26.
19. Casartelli N, Guivel-Benhassine F, Bouziat R, Brandler S, Schwartz O, et al. (2010) The antiviral factor APOBEC3G improves CTL recognition of cultured HIV-infected T cells. J Exp Med 207: 39–49.
20. Jern P, Russell RA, Pathak VK, Coffin JM (2009) Likely role of APOBEC3G-mediated G-to-A mutations in HIV-1 evolution and drug resistance. PLoS Pathog 5: e1000367.
21. Wood N, Bhattacharya T, Keele BF, Giorgi E, Liu M, et al. (2009) HIV evolution in early infection: selection pressures, patterns of insertion and deletion, and the impact of APOBEC. PLoS Pathog 5: e1000414.
22. Nie C, Sato K, Misawa N, Kitayama H, Fujino H, et al. (2009) Selective infection of $CD4^+$ effector memory T lymphocytes leads to preferential depletion of memory T lymphocytes in R5 HIV-1-infected humanized NOD/SCID/IL-$2R\gamma^{null}$ mice. Virology 394: 64–72.

23. Sato K, Izumi T, Misawa N, Kobayashi T, Yamashita Y, et al. (2010) Remarkable lethal G-to-A mutations in *vif*-proficient HIV-1 provirus by individual APOBEC3 proteins in humanized mice. J Virol 84: 9546–9556.
24. Sato K, Koyanagi Y (2011) The mouse is out of the bag: insights and perspectives on HIV-1-infected humanized mouse models. Exp Biol Med 236: 977–985.
25. Sato K, Misawa N, Fukuhara M, Iwami S, An DS, et al. (2012) Vpu augments the initial burst phase of HIV-1 propagation and downregulates BST2 and CD4 in humanized mice. J Virol 86: 5000–5013.
26. Sato K, Misawa N, Nie C, Satou Y, Iwakiri D, et al. (2011) A novel animal model of Epstein-Barr virus-associated hemophagocytic lymphohistiocytosis in humanized mice. Blood 117: 5663–5673.
27. Sato K, Nie C, Misawa N, Tanaka Y, Ito M, et al. (2010) Dynamics of memory and naive $CD8^+$ T lymphocytes in humanized NOD/SCID/IL-$2R\gamma^{null}$ mice infected with CCR5-tropic HIV-1. Vaccine 28 Suppl 2: B32–37.
28. Sato K, Misawa N, Iwami S, Satou Y, Matsuoka M, et al. (2013) HIV-1 Vpr accelerates viral replication during acute infection by exploitation of proliferating $CD4^+$ T cells *in vivo*. PLoS Pathog 9: e1003812.
29. Fitzgibbon JE, Mazar S, Dubin DT (1993) A new type of G→A hypermutation affecting human immunodeficiency virus. AIDS Res Hum Retroviruses 9: 833–838.
30. Gandhi SK, Siliciano JD, Bailey JR, Siliciano RF, Blankson JN (2008) Role of APOBEC3G/F-mediated hypermutation in the control of human immunodeficiency virus type 1 in elite suppressors. J Virol 82: 3125–3130.
31. Janini M, Rogers M, Birx DR, McCutchan FE (2001) Human immunodeficiency virus type 1 DNA sequences genetically damaged by hypermutation are often abundant in patient peripheral blood mononuclear cells and may be generated during near-simultaneous infection and activation of $CD4^+$ T cells. J Virol 75: 7973–7986.
32. Pace C, Keller J, Nolan D, James I, Gaudieri S, et al. (2006) Population level analysis of human immunodeficiency virus type 1 hypermutation and its relationship with APOBEC3G and vif genetic variation. J Virol 80: 9259–9269.
33. Piantadosi A, Humes D, Chohan B, McClelland RS, Overbaugh J (2009) Analysis of the percentage of human immunodeficiency virus type 1 sequences that are hypermutated and markers of disease progression in a longitudinal cohort, including one individual with a partially defective Vif. J Virol 83: 7805–7814.
34. Ulenga NK, Sarr AD, Hamel D, Sankale JL, Mboup S, et al. (2008) The level of APOBEC3G (hA3G)-related G-to-A mutations does not correlate with viral load in HIV type 1-infected individuals. AIDS Res Hum Retroviruses 24: 1285–1290.
35. Vartanian JP, Henry M, Wain-Hobson S (2002) Sustained G→A hypermutation during reverse transcription of an entire human immunodeficiency virus type 1 strain Vau group O genome. J Gen Virol 83: 801–805.
36. Vartanian JP, Meyerhans A, Asjo B, Wain-Hobson S (1991) Selection, recombination, and G→A hypermutation of human immunodeficiency virus type 1 genomes. J Virol 65: 1779–1788.
37. Kijak GH, Janini LM, Tovanabutra S, Sanders-Buell E, Arroyo MA, et al. (2008) Variable contexts and levels of hypermutation in HIV-1 proviral genomes recovered from primary peripheral blood mononuclear cells. Virology 376: 101–111.
38. Russell RA, Pathak VK (2007) Identification of two distinct human immunodeficiency virus type 1 Vif determinants critical for interactions with human APOBEC3G and APOBEC3F. J Virol 81: 8201–8210.
39. Smith JL, Pathak VK (2010) Identification of specific determinants of human APOBEC3F, APOBEC3C, and APOBEC3DE and African green monkey APOBEC3F that interact with HIV-1 Vif. J Virol 84: 12599–12608.
40. Suzuki Y, Koyanagi Y, Tanaka Y, Murakami T, Misawa N, et al. (1999) Determinant in human immunodeficiency virus type 1 for efficient replication under cytokine-induced $CD4^+$ T-helper 1 (Th1)- and Th2-type conditions. J Virol 73: 316–324.
41. Krisko JF, Martinez-Torres F, Foster JL, Garcia JV (2013) HIV restriction by APOBEC3 in humanized mice. PLoS Pathog 9: e1003242.
42. Koning FA, Newman EN, Kim EY, Kunstman KJ, Wolinsky SM, et al. (2009) Defining APOBEC3 expression patterns in human tissues and hematopoietic cell subsets. J Virol 83: 9474–9485.
43. Refsland EW, Stenglein MD, Shindo K, Albin JS, Brown WL, et al. (2010) Quantitative profiling of the full APOBEC3 mRNA repertoire in lymphocytes and tissues: implications for HIV-1 restriction. Nucleic Acids Res 38: 4274–4284.
44. Lepelley A, Louis S, Sourisseau M, Law HK, Pothlichet J, et al. (2011) Innate sensing of HIV-infected cells. PLoS Pathog 7: e1001284.
45. von Sydow M, Sonnerborg A, Gaines H, Strannegard O (1991) Interferon-α and tumor necrosis factor-α in serum of patients in various stages of HIV-1 infection. AIDS Res Hum Retroviruses 7: 375–380.
46. Pillai SK, Abdel-Mohsen M, Guatelli J, Skasko M, Monto A, et al. (2012) Role of retroviral restriction factors in the interferon-α-mediated suppression of HIV-1 in vivo. Proc Natl Acad Sci U S A 109: 3035–3040.
47. Stopak KS, Chiu YL, Kropp J, Grant RM, Greene WC (2007) Distinct patterns of cytokine regulation of APOBEC3G expression and activity in primary lymphocytes, macrophages, and dendritic cells. J Biol Chem 282: 3539–3546.
48. Hultquist JF, Lengyel JA, Refsland EW, LaRue RS, Lackey L, et al. (2011) Human and rhesus APOBEC3D, APOBEC3F, APOBEC3G, and APOBEC3H demonstrate a conserved capacity to restrict Vif-deficient HIV-1. J Virol 85: 11220–11234.
49. Suspene R, Rusniok C, Vartanian JP, Wain-Hobson S (2006) Twin gradients in APOBEC3 edited HIV-1 DNA reflect the dynamics of lentiviral replication. Nucleic Acids Res 34: 4677–4684.
50. Palmer S, Kearney M, Maldarelli F, Halvas EK, Bixby CJ, et al. (2005) Multiple, linked human immunodeficiency virus type 1 drug resistance mutations in treatment-experienced patients are missed by standard genotype analysis. J Clin Microbiol 43: 406–413.
51. Yu Q, Konig R, Pillai S, Chiles K, Kearney M, et al. (2004) Single-strand specificity of APOBEC3G accounts for minus-strand deamination of the HIV genome. Nat Struct Mol Biol 11: 435–442.
52. De Jong JJ, De Ronde A, Keulen W, Tersmette M, Goudsmit J (1992) Minimal requirements for the human immunodeficiency virus type 1 V3 domain to support the syncytium-inducing phenotype: analysis by single amino acid substitution. J Virol 66: 6777–6780.
53. Shioda T, Levy JA, Cheng-Mayer C (1992) Small amino acid changes in the V3 hypervariable region of gp120 can affect the T-cell-line and macrophage tropism of human immunodeficiency virus type 1. Proc Natl Acad Sci U S A 89: 9434–9438.
54. Lengauer T, Sander O, Sierra S, Thielen A, Kaiser R (2007) Bioinformatics prediction of HIV coreceptor usage. Nat Biotechnol 25: 1407–1410.
55. Ebrahimi D, Anwar F, Davenport MP (2012) APOBEC3G and APOBEC3F rarely co-mutate the same HIV genome. Retrovirology 9: 113.
56. Mulder LC, Ooms M, Majdak S, Smedresman J, Linscheid C, et al. (2010) Moderate influence of human APOBEC3F on HIV-1 replication in primary lymphocytes. J Virol 84: 9613–9617.
57. Bishop KN, Holmes RK, Malim MH (2006) Antiviral potency of APOBEC proteins does not correlate with cytidine deamination. J Virol 80: 8450–8458.
58. Holmes RK, Koning FA, Bishop KN, Malim MH (2007) APOBEC3F can inhibit the accumulation of HIV-1 reverse transcription products in the absence of hypermutation. Comparisons with APOBEC3G. J Biol Chem 282: 2587–2595.
59. Bishop KN, Verma M, Kim EY, Wolinsky SM, Malim MH (2008) APOBEC3G inhibits elongation of HIV-1 reverse transcripts. PLoS Pathog 4: e1000231.
60. Gillick K, Pollpeter D, Phalora P, Kim EY, Wolinsky SM, et al. (2013) Suppression of HIV-1 infection by APOBEC3 proteins in primary human $CD4^+$ T cells is associated with inhibition of processive reverse transcription as well as excessive cytidine deamination. J Virol 87: 1508–1517.
61. Kobayashi T, Koizumi Y, Takeuchi JS, Misawa N, Kimura Y, et al. (2014) Quantification of deaminase activity-dependent and -independent restriction of HIV-1 replication mediated by APOBEC3F and APOBEC3G through experimental-mathematical investigation. J Virol 88: 5881–5887.
62. Albin JS, Brown WL, Harris RS (2014) Catalytic activity of APOBEC3F is required for efficient restriction of Vif-deficient human immunodeficiency virus. Virology 450–451: 49–54.
63. Mbisa JL, Bu W, Pathak VK (2010) APOBEC3F and APOBEC3G inhibit HIV-1 DNA integration by different mechanisms. J Virol 84: 5250–5259.
64. Simon V, Zennou V, Murray D, Huang Y, Ho DD, et al. (2005) Natural variation in Vif: differential impact on APOBEC3G/3F and a potential role in HIV-1 diversification. PLoS Pathog 1: e6.
65. Ito M, Hiramatsu H, Kobayashi K, Suzue K, Kawahata M, et al. (2002) NOD/SCID/γ_c^{null} mouse: an excellent recipient mouse model for engraftment of human cells. Blood 100: 3175–3182.
66. An DS, Poon B, Ho Tsong Fang R, Weijer K, Blom B, et al. (2007) Use of a novel chimeric mouse model with a functionally active human immune system to study human immunodeficiency virus type 1 infection. Clin Vaccine Immunol 14: 391–396.
67. Wei X, Decker JM, Liu H, Zhang Z, Arani RB, et al. (2002) Emergence of resistant human immunodeficiency virus type 1 in patients receiving fusion inhibitor (T-20) monotherapy. Antimicrob Agents Chemother 46: 1896–1905.
68. Chiba-Mizutani T, Miura H, Matsuda M, Matsuda Z, Yokomaku Y, et al. (2007) Use of new T-cell-based cell lines expressing two luciferase reporters for accurately evaluating susceptibility to anti-human immunodeficiency virus type 1 drugs. J Clin Microbiol 45: 477–487.
69. Russell RA, Smith J, Barr R, Bhattacharyya D, Pathak VK (2009) Distinct domains within APOBEC3G and APOBEC3F interact with separate regions of human immunodeficiency virus type 1 Vif. J Virol 83: 1992–2003.
70. Izumi T, Io K, Matsui M, Shirakawa K, Shinohara M, et al. (2010) HIV-1 viral infectivity factor interacts with TP53 to induce G2 cell cycle arrest and positively regulate viral replication. Proc Natl Acad Sci U S A 107: 20798–20803.
71. Sato K, Aoki J, Misawa N, Daikoku E, Sano K, et al. (2008) Modulation of human immunodeficiency virus type 1 infectivity through incorporation of tetraspanin proteins. J Virol 82: 1021–1033.
72. Sabbah A, Chang TH, Harnack R, Frohlich V, Tominaga K, et al. (2009) Activation of innate immune antiviral responses by Nod2. Nat Immunol 10: 1073–1080.
73. Thompson JD, Higgins DG, Gibson TJ (1994) CLUSTAL W: improving the sensitivity of progressive multiple sequence alignment through sequence weighting, position-specific gap penalties and weight matrix choice. Nucleic Acids Res 22: 4673–4680.
74. Tamura K, Peterson D, Peterson N, Stecher G, Nei M, et al. (2011) MEGA5: molecular evolutionary genetics analysis using maximum likelihood, evolutionary distance, and maximum parsimony methods. Mol Biol Evol 28: 2731–2739.
75. Darriba D, Taboada GL, Doallo R, Posada D (2012) jModelTest 2: more models, new heuristics and parallel computing. Nat Methods 9: 772.

76. Tamura K, Nei M (1993) Estimation of the number of nucleotide substitutions in the control region of mitochondrial DNA in humans and chimpanzees. Mol Biol Evol 10: 512–526.
77. Criscuolo A (2011) morePhyML: improving the phylogenetic tree space exploration with PhyML 3. Mol Phylogenet Evol 61: 944–948.
78. Johnson VA, Calvez V, Gunthard HF, Paredes R, Pillay D, et al. (2011) 2011 update of the drug resistance mutations in HIV-1. Top Antivir Med 19: 156–164.
79. Guo Y, Dong L, Qiu X, Wang Y, Zhang B, et al. (2014) Structural basis for hijacking CBF-β and CUL5 E3 ligase complex by HIV-1 Vif. Nature 505: 229–233.
80. Perelson AS, Essunger P, Cao Y, Vesanen M, Hurley A, et al. (1997) Decay characteristics of HIV-1-infected compartments during combination therapy. Nature 387: 188–191.
81. Markowitz M, Louie M, Hurley A, Sun E, Di Mascio M, et al. (2003) A novel antiviral intervention results in more accurate assessment of human immunodeficiency virus type 1 replication dynamics and T-cell decay *in vivo*. J Virol 77: 5037–5038.

ELSEVIER

CrossMark

Institut Pasteur

Microbes and Infection 16 (2014) 936–944

www.elsevier.com/locate/micinf

Original article

Distinct combinations of amino acid substitutions in *N*-terminal domain of Gag-capsid afford HIV-1 resistance to rhesus TRIM5α

Masako Nomaguchi [a], Emi E. Nakayama [b], Masaru Yokoyama [c], Naoya Doi [a,d], Tatsuhiko Igarashi [e], Tatsuo Shioda [b], Hironori Sato [c], Akio Adachi [a,*]

[a] *Department of Microbiology, Institute of Health Biosciences, The University of Tokushima Graduate School, Tokushima, Tokushima, Japan*
[b] *Department of Viral Infections, Research Institute for Microbial Diseases, Osaka University, Suita, Osaka, Japan*
[c] *Laboratory of Viral Genomics, Pathogen Genomics Center, National Institute of Infectious Diseases, Musashimurayama, Tokyo, Japan*
[d] *Japanese Foundation for AIDS Prevention, Chiyoda-ku, Tokyo, Japan*
[e] *Laboratory of Primate Model, Experimental Research Center for Infectious Diseases, Institute for Virus Research, Kyoto University, Kyoto, Kyoto, Japan*

Received 18 June 2014; accepted 27 August 2014
Available online 4 September 2014

Abstract

TRIM5α is a potent anti-retroviral factor that interacts with viral capsid (CA) in a species-specific manner. Recently, we and others reported generation of two distinct HIV-1 CAs that effectively overcome rhesus TRIM5α-imposed species barrier. In this study, to directly compare the effect of different mutations in the two HIV-1 CAs on evasion from macaque TRIM5-restriction, we newly generated macaque-tropic HIV-1 (HIV-1mt) proviral clones carrying the distinct CAs in the same genomic backbone, and examined their replication abilities in macaque TRIM5-overexpressing human cells and in rhesus cells. Comparative analysis of amino acid sequences and homology modeling-based structures revealed that, while both CAs gained some mutated amino acids with similar physicochemical properties, their overall appearances of N-terminal domains were different. Experimentally, the two CAs exhibited incomplete TRIM5α-resistance relative to SIVmac239 CA and different degrees of susceptibility to various TRIM5 proteins. Finally, two HIV-1mt clones carrying a different combination of the CA mutations were found to grow to a comparable extent in established and primary rhesus cells. Our data show that there could be some distinct CA patterns to confer significant TRIM5-resistance on HIV-1.

Keywords: HIV-1; HIV-1mt; Capsid; Gag-CA; Rhesus macaque; TRIM5α

1. Introduction

TRIM5α interacts with retroviral Gag-capsid (CA) and inhibits viral replication in a species-specific manner [1–6]. TRIM5α acts as a pattern-recognition molecule via its C-terminal B30.2/SPRY domain on diverse retroviral CAs [7–12]. It is proposed that retroviruses overcome TRIM5α-restriction either by mutating CA to abolish recognition by TRIM5α B30.2/SPRY domain, or by altering a surface pattern of CA lattice [9]. Macaque TRIM5α is one of the major species-barriers for HIV-1. Evasion from macaque TRIM5α-restriction would facilitate establishing HIV-1/macaque models useful for basic and clinical AIDS studies [13,14]. Recently, we successfully generated rhesus macaque (RhM) TRIM5α-resistant HIV-1 CA, designated LSDQ (Fig. 1A), through comparative sequence/structure analyses of HIV and SIVmac239 CAs [15]. Soll et al. also constructed RhM TRIM5α-resistant HIV-1 CA, designated LNEIE (Fig. 1A), by "assisted evolution" method [16]. Interestingly, LSDQ and LNEIE CAs have different amino acid substitutions that contribute to TRIM5α-resistance. Furthermore, a virus carrying LSDQ CA or LNEIE CA grew best in RhM peripheral blood

* Corresponding author. Tel.: +81 88 633 7078; fax: +81 88 633 7080.
E-mail address: adachi@basic.med.tokushima-u.ac.jp (A. Adachi).

http://dx.doi.org/10.1016/j.micinf.2014.08.017
1286-4579/